geopress

Rainfall:
State of the Science

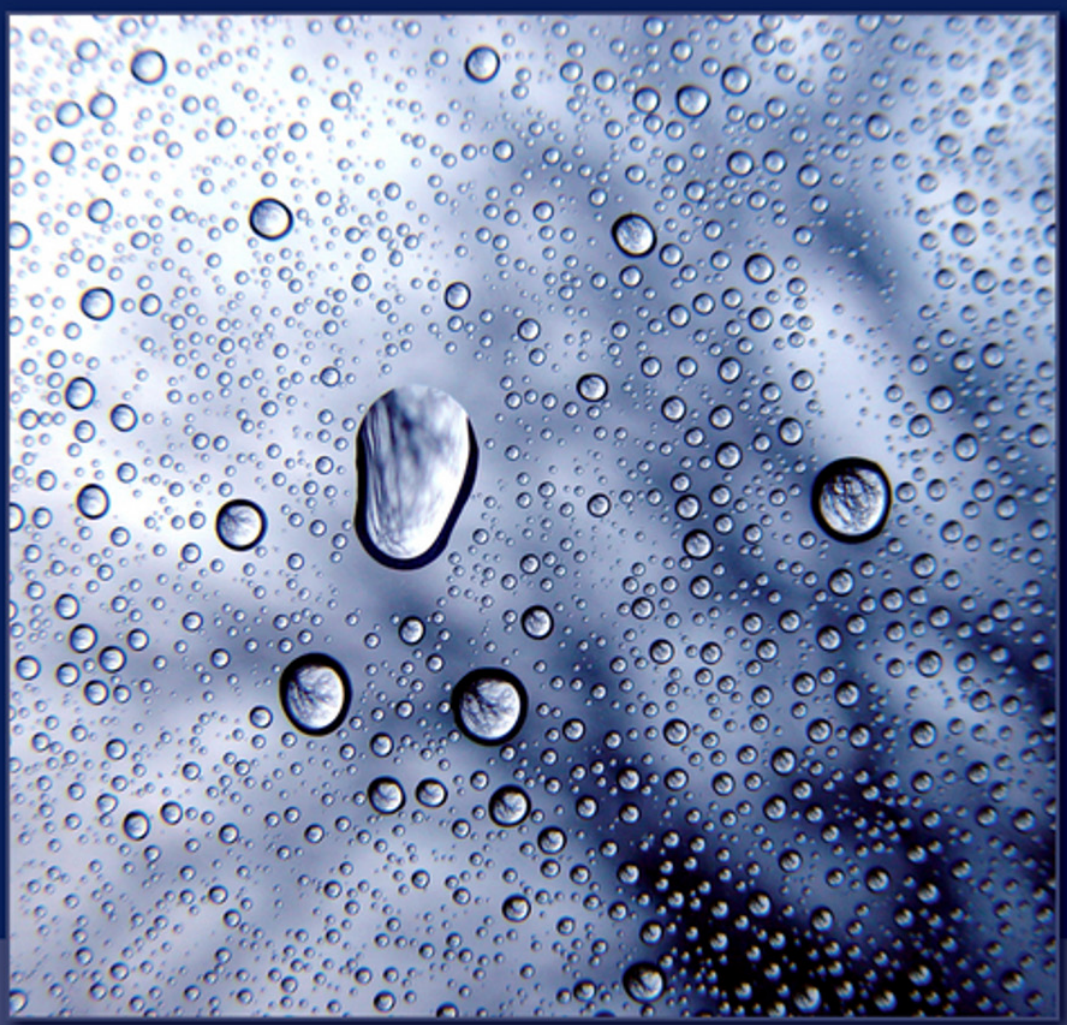

Firat Y. Testik and Mekonnen Gebremichael
Editors

AGU
American Geophysical Union

Geophysical Monograph Series

Including
IUGG Volumes
Maurice Ewing Volumes
Mineral Physics Volumes

156 **Particle Acceleration in Astrophysical Plasmas: Geospace and Beyond** *Dennis Gallagher, James Horwitz, Joseph Perez, Robert Preece, and John Quenby (Eds.)*

157 **Seismic Earth: Array Analysis of Broadband Seismograms** *Alan Levander and Guust Nolet (Eds.)*

158 **The Nordic Seas: An Integrated Perspective** *Helge Drange, Trond Dokken, Tore Furevik, Rüdiger Gerdes, and Wolfgang Berger (Eds.)*

159 **Inner Magnetosphere Interactions: New Perspectives From Imaging** *James Burch, Michael Schulz, and Harlan Spence (Eds.)*

160 **Earth's Deep Mantle: Structure, Composition, and Evolution** *Robert D. van der Hilst, Jay D. Bass, Jan Matas, and Jeannot Trampert (Eds.)*

161 **Circulation in the Gulf of Mexico: Observations and Models** *Wilton Sturges and Alexis Lugo-Fernandez (Eds.)*

162 **Dynamics of Fluids and Transport Through Fractured Rock** *Boris Faybishenko, Paul A. Witherspoon, and John Gale (Eds.)*

163 **Remote Sensing of Northern Hydrology: Measuring Environmental Change** *Claude R. Duguay and Alain Pietroniro (Eds.)*

164 **Archean Geodynamics and Environments** *Keith Benn, Jean-Claude Mareschal, and Kent C. Condie (Eds.)*

165 **Solar Eruptions and Energetic Particles** *Natchimuthukonar Gopalswamy, Richard Mewaldt, and Jarmo Torsti (Eds.)*

166 **Back-Arc Spreading Systems: Geological, Biological, Chemical, and Physical Interactions** *David M. Christie, Charles Fisher, Sang-Mook Lee, and Sharon Givens (Eds.)*

167 **Recurrent Magnetic Storms: Corotating Solar Wind Streams** *Bruce Tsurutani, Robert McPherron, Walter Gonzalez, Gang Lu, José H. A. Sobral, and Natchimuthukonar Gopalswamy (Eds.)*

168 **Earth's Deep Water Cycle** *Steven D. Jacobsen and Suzan van der Lee (Eds.)*

169 **Magnetospheric ULF Waves: Synthesis and New Directions** *Kazue Takahashi, Peter J. Chi, Richard E. Denton, and Robert L. Lysal (Eds.)*

170 **Earthquakes: Radiated Energy and the Physics of Faulting** *Rachel Abercrombie, Art McGarr, Hiroo Kanamori, and Giulio Di Toro (Eds.)*

171 **Subsurface Hydrology: Data Integration for Properties and Processes** *David W. Hyndman, Frederick D. Day-Lewis, and Kamini Singha (Eds.)*

172 **Volcanism and Subduction: The Kamchatka Region** *John Eichelberger, Evgenii Gordeev, Minoru Kasahara, Pavel Izbekov, and Johnathan Lees (Eds.)*

173 **Ocean Circulation: Mechanisms and Impacts—Past and Future Changes of Meridional Overturning** *Andreas Schmittner, John C. H. Chiang, and Sidney R. Hemming (Eds.)*

174 **Post-Perovskite: The Last Mantle Phase Transition** *Kei Hirose, John Brodholt, Thorne Lay, and David Yuen (Eds.)*

175 **A Continental Plate Boundary: Tectonics at South Island, New Zealand** *David Okaya, Tim Stem, and Fred Davey (Eds.)*

176 **Exploring Venus as a Terrestrial Planet** *Larry W. Esposito, Ellen R. Stofan, and Thomas E. Cravens (Eds.)*

177 **Ocean Modeling in an Eddying Regime** *Matthew Hecht and Hiroyasu Hasumi (Eds.)*

178 **Magma to Microbe: Modeling Hydrothermal Processes at Oceanic Spreading Centers** *Robert P. Lowell, Jeffrey S. Seewald, Anna Metaxas, and Michael R. Perfit (Eds.)*

179 **Active Tectonics and Seismic Potential of Alaska** *Jeffrey T. Freymueller, Peter J. Haeussler, Robert L. Wesson, and Göran Ekström (Eds.)*

180 **Arctic Sea Ice Decline: Observations, Projections, Mechanisms, and Implications** *Eric T. DeWeaver, Cecilia M. Bitz, and L.-Bruno Tremblay (Eds.)*

181 **Midlatitude Ionospheric Dynamics and Disturbances** *Paul M. Kintner, Jr., Anthea J. Coster, Tim Fuller-Rowell, Anthony J. Mannucci, Michael Mendillo, and Roderick Heelis (Eds.)*

182 **The Stromboli Volcano: An Integrated Study of the 2002–2003 Eruption** *Sonia Calvari, Salvatore Inguaggiato, Giuseppe Puglisi, Maurizio Ripepe, and Mauro Rosi (Eds.)*

183 **Carbon Sequestration and Its Role in the Global Carbon Cycle** *Brian J. McPherson and Eric T. Sundquist (Eds.)*

184 **Carbon Cycling in Northern Peatlands** *Andrew J. Baird, Lisa R. Belyea, Xavier Comas, A. S. Reeve, and Lee D. Slater (Eds.)*

185 **Indian Ocean Biogeochemical Processes and Ecological Variability** *Jerry D. Wiggert, Raleigh R. Hood, S. Wajih A. Naqvi, Kenneth H. Brink, and Sharon L. Smith (Eds.)*

186 **Amazonia and Global Change** *Michael Keller, Mercedes Bustamante, John Gash, and Pedro Silva Dias (Eds.)*

187 **Surface Ocean–Lower Atmosphere Processes** *Corinne Le Quèrè and Eric S. Saltzman (Eds.)*

188 **Diversity of Hydrothermal Systems on Slow Spreading Ocean Ridges** *Peter A. Rona, Colin W. Devey, Jérôme Dyment, and Bramley J. Murton (Eds.)*

189 **Climate Dynamics: Why Does Climate Vary?** *De-Zheng Sun and Frank Bryan (Eds.)*

190 **The Stratosphere: Dynamics, Transport, and Chemistry** *L. M. Polvani, A. H. Sobel, and D. W. Waugh (Eds.)*

geopress

Geophysical Monograph 191

Rainfall: State of the Science

Firat Y. Testik
Mekonnen Gebremichael
Editors

American Geophysical Union
Washington, DC

Published under the aegis of the AGU Books Board

Kenneth R. Minschwaner, Chair; Gray E. Bebout, Joseph E. Borovsky, Kenneth H. Brink, Ralf R. Haese, Robert B. Jackson, W. Berry Lyons, Thomas Nicholson, Andrew Nyblade, Nancy N. Rabalais, A. Surjalal Sharma, and Darrell Strobel, members.

Library of Congress Cataloging-in-Publication Data

Rainfall : state of the science / Firat Y. Testik and Mekonnen Gebremichael, editors.
p. cm. — (Geophysical monograph, ISSN 0065-8448 ; 191)
Includes bibliographical references and index.
ISBN 978-0-87590-481-8 (alk. paper)
1. Rain and rainfall. 2. Rainfall probabilities. 3. Rain and rainfall—Measurement. I. Testik, Firat Y., 1977- II. Gebremichael, Mekonnen.
QC925.R24 2010
551.57'7—dc22

2010049230

ISBN: 978-0-87590-481-8
ISSN: 0065-8448

Cover Image: Raindrops on a window.

Printed in the United States of America.

CONTENTS

PREFACE

Rainfall, liquid precipitation, is a critical component of water and energy cycles. It is a critical source of fresh water, sustaining life on Earth, and an important process for energy exchanges between the atmosphere, ocean, and land, determining Earth's climate. It is central to water supply, agriculture, natural ecosystems, hydroelectric power, industry, drought, flood, and disease hazards for example. Therefore, rainfall is at the heart of social, economical, and political challenges in today's world. It is a high priority to use advancements in scientific knowledge of rainfall to develop solutions to the water-related challenges faced by society. The three main aspects of rainfall, "rainfall microphysics," "rainfall measurement and estimation," and "rainfall statistical analyses," have been widely studied as individual topics over the years. It is the goal of this book to synthesize all of these aspects to provide an integral picture of the state of the science of rainfall.

This book presents the state of the science of rainfall focusing on three areas: (1) rainfall microphysics, (2) rainfall measurement and estimation, and (3) rainfall statistical analyses. Each part consists of a number of self-contained chapters providing three forms of information: fundamental principles, detailed overview of current knowledge and description of existing methods, and emerging techniques and future research directions. Each book chapter is authored by preeminent researchers in their respective fields and has been reviewed by two renowned researchers within the same field for the scientific accuracy, quality, and completeness of the final content. The book is tailored to be an indispensable reference for researchers, practitioners, and graduate students who study any aspect of rainfall or utilize rainfall information in various science and engineering disciplines.

As editors of this book, we would like to express our utmost gratitude to everyone who has contributed in this publication. We are thankful to all the chapter authors for contributing their expertise and time. We are thankful also to all the reviewers who have selflessly served for the success of this project.

Firat Y. Testik
Clemson University

Mekonnen Gebremichael
University of Connecticut

Rainfall: State of the Science
Geophysical Monograph Series 191

10.1029/2010GM001026

Microphysics, Measurement, and Analyses of Rainfall

Mekonnen Gebremichael

Department of Civil and Environmental Engineering, University of Connecticut, Storrs, Connecticut, USA

Firat Y. Testik

Department of Civil Engineering, Clemson University, Clemson, South Carolina, USA

Rainfall, liquid precipitation, is a critical component of water and energy cycles. It is a critical source of water for water supply, agriculture, natural ecosystems, hydroelectric power, and industry and is central to issues of drought, flood, and disease hazards. The most desired characteristic of rainfall is the rainfall rate at Earth's surface. This book, "*Rainfall: State of the Science*," aims to synthesize the three main aspects (microphysics, measurement and estimation, and statistical analyses) of rainfall rate estimation efforts to provide an integral picture of this endeavor. In this introductory chapter, we present the issues that will be discussed in detail in the subsequent chapters.

1. MICROPHYSICS

Understanding the microphysics of rainfall is important to accurately estimate rainfall rate from microwave remote sensing and to model the rainfall process in process-based models. Rainfall microphysics, deals with the dynamical processes for individual and populated raindrops throughout their journey from cloud to surface. Rainfall and cloud microstructure is a broad topic, and there are several comprehensive books [*Pruppacher and Klett*, 1978; *Rogers and Yau*, 1989; *Mason*, 1971] devoted to this subject. For the purpose of rainfall rate retrievals, accurate information on the raindrop shape, fall velocity, and raindrop size distribution (DSD) are of particular interest. Therefore, main considerations on rainfall microphysics discussions in this book will be centered on these quantities with a perspective from rainfall rate retrievals. Aside from rainfall rate measurements, these quantities have important applications such as soil erosion studies [*Fox*, 2004; *Fornis et al.*, 2005], air pollution studies [*Mircea et al.*, 2000], and telecommunications [*Panagopoulos and Kanellopoulos*, 2002].

Raindrops demonstrate a variety of complex shapes and shape-altering oscillations under the action of a range of surface and body forces. Shapes and fall velocities of raindrops are closely coupled resulting in a dynamic interplay until equilibrium is reached. Raindrop shapes and fall velocities are important input parameters for extracting rainfall information via remote sensing. Polarimetric weather radars utilize vertical to horizontal chord ratios of "equilibrium" raindrop shapes and corresponding "terminal" fall velocities. Consequently, there have been a number of studies on raindrop morphodynamics (i.e., static and dynamic processes related to raindrop shape) over the years [*Laws*, 1941; *Spilhaus*, 1948; *Gunn*, 1949; *Gunn and Kinzer*, 1949; *Savic*, 1953; *McDonald*, 1954; *Pruppacher and Pitter*, 1971; *Green*, 1975; *Wang and Pruppacher*, 1977; *Beard*, 1977; *Beard and Chuang*, 1987; *Beard et al.*, 1989]. *Jones et al.* [this volume] review raindrop morphodynamics, providing a synthesis of information on raindrop shape and related physical processes, including forces shaping the raindrops, raindrop oscillations, and fall velocities.

Rainfall: State of the Science
Geophysical Monograph Series 191

10.1029/2010GM001025

Raindrops are formed within clouds through collisional interactions of cloud droplets. After formation, raindrops interact with each other via collisions throughout their journey from cloud to surface. These collisions may result in coalescence, breakup, and bounce of colliding drops. As a result of these collision outcomes, DSD continuously evolves with height. Accurate information on DSD at different heights is important for obtaining accurate rainfall information via remote sensing. Numerical simulations based on the stochastic coalescence/breakup equation and laboratory models of governing processes [*Low and List*, 1982a, 1982b] are used to obtain information on the DSD evolution with height [e.g., *Gillespie and List*, 1978; *List and McFarquhar*, 1990; *McFarquhar*, 2004]. *Beheng* [this volume] discusses the formation of raindrops from cloud droplets and collisional interactions of raindrops that result in an evolution of the raindrop size distribution. Environmental interactions are omitted.

Following the landmark study by *Marshall and Palmer* [1948], various distributions have been used to represent DSD, including exponential, Gaussian, and lognormal distributions. The assumed form of DSD plays a critical role in rainfall rate retrieval from both ground- and space-based systems. Various numerical simulations of DSD evolution under the action of collisional interactions have shown evidence for an equilibrium form of DSD after sufficient evolution time is given [e.g., *Valdez and Young*, 1985; *List et al.*, 1987; *List and McFarquhar*, 1990; *Hu and Srivastava*, 1995]. However, field observations have not verified the occurrence of an equilibrium DSD as predicted by these numerical simulations. *McFarquhar* [this volume] provides an overview of observed raindrop size distributions at both the ground and aloft as well as the evolution of the raindrop size distributions throughout the rain shaft from numerical simulations.

2. MEASUREMENT AND ESTIMATION

Information on rainfall properties can be obtained by means of different observing systems and associated algorithms: direct in situ sensors (i.e., rain gauges and disdrometers), ground-based remote sensors (i.e., weather radars), and space-based remote sensors (i.e., radars and infrared sensors). Each sensor has its own strengths and limitations.

Rain gauges and disdrometers provide direct in situ point measurements of rainfall properties at high temporal resolution. Rain gauge measurements of rainfall rate continue to be the main basis for "calibrating" rainfall remote sensing algorithms and for numerous research and operational applications that require rainfall data. However, even at their point measurement scales, rain gauge rainfall measurements are subject to systematic and random measurement errors, the most important of which are the following: the drift of rainfall particles due to wind field deformation around the gauge, losses caused by wetting of the inner walls of the gauge, evaporation of water accumulated in the gauge container, splashing of raindrops out or into the gauge, calibration-related errors, malfunctioning problems, poor location selection, and local random errors. Disdrometers measure DSD that describes the rainfall microstructure. The DSD data have been widely used in studying soil erosion and rainfall microphysical properties and, perhaps most importantly, derivation of radar rainfall retrieval algorithms. The DSD measurements can be affected by various sources of errors, which can be grouped into instrumental, sampling, and observational errors. *Habib et al.* [this volume] present an overview of the different types of rain gauges and disdrometers, discuss the major sources of uncertainties that contaminate measurements at the local point scale, and describe the recently developed methods for automatic quality control of the rain gauge data.

The availability of rainfall estimates from conventional ground-based scanning weather radars (i.e., single-polarization radar systems), such as the U.S. Weather Surveillance Radars-1988 Doppler (WSR-88D) radars, at high space-time resolutions and over large areas has greatly advanced our quantitative information on the space-time variability of rainfall. However, because radar measures volumetric reflectivity of hydrometeors aloft rather than rainfall near the ground, radar rainfall estimation is inherently subject to various sources of error. The major sources and possible practical consequences of these errors have been well recognized and discussed by many researchers [e.g., *Wilson and Brandes*, 1979; *Zawadzki*, 1982; *Austin*, 1987; *Krajewski and Smith*, 2002; *Jordan et al.*, 2003; *Krajewski et al.*, 2010]. Recent work on improving the accuracy of rainfall estimates from conventional weather radars consists of incorporating rain gauge measurements to remove the bias in the radar rainfall estimates and using multiple radar rainfall fields whenever possible. *Seo et al.* [this volume] describe the foundations of radar and multisensor rainfall estimation, recent advances and notable applications, and outstanding issues and areas of research that must be addressed to meet the needs of forecasting in various applications such as hydrology.

As part of the modernization of the WSR-88D, the U.S. National Weather Service and other agencies have decided to add a polarimetric capability to existing conventional single-polarization radars. Dual polarization provides additional information compared to single-polarization radar systems, which helps to significantly improve the accuracy of radar rainfall estimates. The three polarimetric variables that are

often used in rainfall estimation are the radar reflectivity at horizontal polarization, the differential reflectivity (defined as the difference between reflectivities at horizontal and vertical polarizations), and the differential phase (defined as the difference between the phases of the radar signals at orthogonal polarizations). An overview of the methods of rainfall estimation from these variables is presented by *Cifelli and Chandrasekar* [this volume].

Remote sensing from a space platform provides a unique opportunity to obtain spatial fields of rainfall information over large areas of Earth. During the last two decades, satellite-based instruments have been designed to collect observations mainly at thermal infrared (IR) and microwave (MW) wavelengths that can be used to estimate rainfall rates. Observations in the IR band are available in passive modes from (near) polar orbiting (revisit times of 1–2 days) and geostationary orbits (revisit times of 15–30 min), while observations in the passive and active MW band are only available from the (near) polar-orbiting satellites. A number of algorithms have been developed to estimate rainfall rates by combining information from the more accurate (but less frequent) MW observations with the more frequent (but less accurate) IR observations to take advantage of the complementary strengths [*Sorooshian et al.*, 2000; *Scofield and Kuligowski*, 2003; *Joyce et al.*, 2004; *Turk and Miller*, 2005; *Huffman et al.*, 2007; *Ushio and Kachi*, 2010]. Satellite rainfall estimates are subject to a variety of error sources (gaps in revisiting times, poor direct relationship between MW cloud top measurements and rainfall rate, atmospheric effects that modify the radiation field, etc.). The errors increase with increasing space-time resolution and depend largely on the algorithm technique, type, and number of satellite sensors used and the study region [e.g., *Hong et al.*, 2004; *Gottschalck et al.*, 2005; *Brown*, 2006; *Ebert et al.*, 2007; *Tian et al.*, 2007; *Bitew and Gebremichael*, 2010; *Dinku et al.*, 2010; *Sapiano et al.*, 2010]. Ongoing research and development continues to address the accuracy and the resolution (temporal and spatial) of these estimates. *Kidd et al.* [this volume] cover the basis of the satellite systems used in the observation of rainfall and the processing of these measurements to generate rainfall estimates, discuss research challenges, and provide research and development recommendations.

3. STATISTICAL ANALYSES

Various statistical techniques are often applied to rainfall data depending on the application and source of data. Commonly employed statistical analyses are extreme event analysis, spatial interpolation of point rainfall, rainfall generation, and uncertainty analysis of remote sensing rainfall estimates.

Statistical analysis of extreme rainfall events is useful for a number of engineering applications including hydraulic design (culverts and storm sewers) and landslide hazard evaluations. Intensity-duration-frequency (IDF) curves, with areal reduction factors, are commonly used for design storm calculations. For any prescribed rainfall duration (which depends on the time of concentration for the watershed) and return period (which is often set as a standard value depending on the purpose and failure consequence of the hydraulic structure), the corresponding design rainfall intensity is obtained from regional IDF curves. The common method of developing IDF consists of the following steps: getting the annual maximum series of rainfall intensity for a given duration, using distributions (parametric or nonparametric) to find rainfall intensity for different return periods, and repeating the above steps for different durations. This method has recently come under criticism as it conveniently ignores the joint probability distribution among the rainfall characteristics: depth, intensity, and duration. The difficulty in modeling the joint distributions is that most parametric multivariate distributions are unable to handle rainfall because of the heavy-tailed distributions in the rainfall characteristics. The recently emerging technique of copula [*Sklar*, 1959] has shown promise in overcoming this difficulty because of its ability to model the dependence structure independently of the marginal distributions. Recent studies have successfully used the copula technique to model the joint distribution among rainfall depth, intensity, and duration [*De Michele and Salvadori*, 2003; *Salvadori and De Michele*, 2004a, 2004b; *Zhang and Singh*, 2007; *Kao and Govindaraju*, 2007, 2008; *Wang et al.*, 2010]. *Durrans* [this volume] presents an overview of the historical development of IDF, common methods for constructing IDF, and emerging new methods.

The frequency (or return period) analysis of extreme events is important to develop IDF curves and to test for any trends in the extremes. A number of parametric distributions (Gumbel, generalized extreme value, lognormal, log-Pearson type 3, Halphen, and generalized logistics) have been developed over the years to model the extreme rainfall events. There are two main statistical approaches to fit these distributions. The first approach applies to annual maxima of time series. The second approach looks at exceedances over high threshold, also known as the "peaks over threshold" approach. Prior to any statistical analyses, the data need to be checked for any outlier, dependence, and stationarity. Focusing on the first approach, *El Adlouni and Ouarda* [this volume] present detailed information on data preparation (detection and treatment of outliers, independence, and stationarity), the parametric distributions (and associated parameter estimation techniques) in the case of stationary time series, and modeling of nonstationary time series.

Spatial rainfall analysis is performed to estimate areal rainfall from point rain gauge data, or to estimate rainfall value at a site based on rainfall measured at another site and auxiliary information, or to generate a spatial pattern. *Hengl et al.* [this volume] present the spatial analysis techniques used in rainfall, with programming codes to help interested users apply the techniques. Stochastic rainfall generation is performed to generate long time series of rainfall data for a variety of applications including probabilistic failure assessment of natural or man-made systems where rain is an important input. *Sharma and Mehrotra* [this volume] present an overview of stochastic generation of rainfall, with a focus on daily and subdaily rainfall generation at point and multiple locations, for the current climate assuming climatic stationarity, as well as for future climates using exogenous inputs simulated using general circulation models under assumed greenhouse gas emission scenarios.

Remote sensing rainfall estimates are subject to systematic and random errors from various sources, some of which are inherent to the observation system and are unavoidable. Operational remote sensing rainfall products are deterministic and do not contain quantitative information on the level of the estimation errors. This has led to the current situation in which those who use remote sensing rainfall estimates know that there are significant errors in the estimates, but they have no quantitative information about the magnitudes of the estimation errors. Consequently, there are no mechanisms to account for the uncertainty of remote sensing rainfall estimates in applications and decision making. A possible solution to this major problem is to construct an error model that characterizes the conditional distribution of actual rainfall rate for any given remote sensing rainfall estimate. *Mandapaka and Germann* [this volume] present the advances in the area of weather radar rainfall error modeling that have taken place over the past decade. Compared to weather radar rainfall estimates, the satellite rainfall estimates are subject to additional error sources and therefore have higher estimation errors. *Gebremichael* [this volume] presents a recommended standard framework for quantifying errors in satellite rainfall estimates, reviews existing error models and presents emerging ones, and performs quantitative assessment of the utility of satellite rainfall estimates for hydrological applications in selected regions.

REFERENCES

Austin, P. M. (1987), Relation between measured radar reflectivity and surface rainfall, *Mon. Weather Rev.*, *115*, 1053–1071.

Beard, K. V. (1977), On the acceleration of large water drops to terminal velocity, *J. Appl. Meteorol.*, *16*, 1068–1071.

Beard, K. V., and C. Chuang (1987), A new model for the equilibrium shape of raindrops, *J. Atmos. Sci.*, *44*(11), 1509–1525.

Beard, K. V., H. T. Ochs, III, and R. J. Kubesh (1989), Natural oscillations of small raindrops, *Nature*, *342*, 408–410.

Beheng, K. D. (2010), The evolution of raindrop spectra: A review of microphysical essentials, in *Rainfall: State of the Science*, *Geophys. Monogr. Ser.*, doi:10.1029/2010GM000957, this volume.

Bitew, M. M., and M. Gebremichael (2010), Evaluation through independent measurements: Complex terrain and humid tropical region in Ethiopia, in *Satellite Rainfall Applications for Surface Hydrology*, edited by M. Gebremichael and F. Hossain, pp. 205–214, doi:10.1007/978-90-481-2915-7_12, Springer, New York.

Brown, J. E. M. (2006), An analysis of the performance of hybrid infrared and microwave satellite precipitation algorithms over India and adjacent regions, *Remote Sens. Environ.*, *101*, 63–81.

Cifelli, R., and V. Chandrasekar (2010), Dual-polarization radar rainfall estimation, in *Rainfall: State of the Science*, *Geophys. Monogr. Ser.*, doi:10.1029/2010GM000930, this volume.

De Michele, C., and G. Salvadori (2003), A generalized Pareto intensity-duration model of storm rainfall exploiting 2-copulas, *J. Geophys. Res.*, *108*(D2), 4067, doi:10.1029/2002JD002534.

Dinku, T., S. J. Connor, and P. Ceccato (2010), Comparison of CMORPH and TRMM-3B42 over mountainous regions of Africa and South America, in *Satellite Rainfall Applications for Surface Hydrology*, edited by M. Gebremichael and F. Hossain, pp. 193–204, doi:10.1007/978-90-481-2915-7_11, Springer, New York.

Durrans, S. R. (2010), Intensity-duration-frequency curves, in *Rainfall: State of the Science*, *Geophys. Monogr. Ser.*, doi: 10.1029/2009GM000919, this volume.

Ebert, E. E., J. E. Janowiak, and C. Kidd (2007), Comparison of near-real-time precipitation estimates from satellite observations and numerical models, *Bull. Am. Meteorol. Soc.*, *88*, 47–64.

El Adlouni, S., and T. B. M. J. Ouarda (2010), Frequency analysis of extreme rainfall events, in *Rainfall: State of the Science*, *Geophys. Monogr. Ser.*, doi:10.1029/2010GM000976, this volume.

Fornis, R. L., H. R. Vermeulen, and J. D. Nieuwenhuis (2005), Kinetic energy-rainfall intensity relationship for central Cebu, Philippines for soil erosion studies, *J. Hydrol.*, *300*, 20–32.

Fox, N. I. (2004), The representation of rainfall drop-size distribution and kinetic energy, *Hydrol. Earth Syst. Sci.*, *8*(5), 1001–1007.

Gebremichael, M. (2010), Framework for satellite rainfall product evaluation, in *Rainfall: State of the Science*, *Geophys. Monogr. Ser.*, doi:10.1029/2010GM000974, this volume.

Gillespie, J. R., and R. List (1978), Effects of collision-induced breakup on drop size evolution in steady state rainshafts, *Pure Appl. Geophys.*, *117*, 599–626.

Gottschalck, J., J. Meng, M. Rodell, and P. Houser (2005), Analysis of multiple precipitation products and preliminary assessment of their impact on global land data assimilation system land surface states, *J. Hydrometeorol.*, *6*, 573–598.

Green, A. E. (1975), An approximation for the shapes of large raindrops, *J. Appl. Meteorol.*, *14*, 1578–1583.

Gunn, R. (1949), Mechanical resonance in freely falling raindrops, *J. Geophys. Res.*, *54*, 383–385.

Gunn, R., and G. D. Kinzer (1949), The terminal velocity of fall for water droplets in stagnant air, *J. Meteorol.*, *6*, 243–248.

Habib, E., G. Lee, D. Kim, and G. J. Ciach (2010), Ground-based direct measurement, in *Rainfall: State of the Science*, *Geophys. Monogr. Ser.*, doi:10.1029/2010GM000953, this volume.

Hengl, T., A. AghaKouchak, and M. P. Tadić (2010), Methods and data sources for spatial prediction of rainfall, in *Rainfall: State of the Science*, *Geophys. Monogr. Ser.*, doi:10.1029/2010GM000999, this volume.

Hong, Y., K. L. Hsu, S. Sorooshian, and X. Gao (2004), Precipitation estimation from remotely sensed imagery using an artificial neural network cloud classification system, *J. Appl. Meteorol.*, *43*, 1834–1852.

Hu, Z., and R. C. Srivastava (1995), Evolution of raindrop size distribution by coalescence, breakup, and evaporation: Theory and observations, *J. Atmos. Sci.*, *52*(10), 1761–1783.

Huffman, G. J., R. F. Adler, D. T. Bolvin, G. Gu, E. J. Nelkin, K. P. Bowman, Y. Hong, E. F. Stocker, and D. B. Wolff (2007), The TRMM Multisatellite Precipitation Analysis (TMPA): Quasi-global, multilayer, combined-sensor, precipitation estimates at fine scale, *J. Hydrometeorol.*, *8*, 38–55.

Jones, B. K., J. R. Saylor, and F. Y. Testik (2010), Raindrop morphodynamics, in *Rainfall: State of the Science*, *Geophys. Monogr. Ser.*, doi:10.1029/2009GM000928, this volume.

Jordan, P. W., A. W. Seed, and P. E. Wienmann (2003), A stochastic model of radar measurement errors in rainfall accumulations at catchment scale, *J. Hydrometeorol.*, *4*, 841–855.

Joyce, R. J., J. E. Janowiak, P. A. Arkin, and P. Xie (2004), CMORPH: A method that produces global precipitation estimates from passive microwave and infrared data at high spatial and temporal resolution, *J. Hydrometeorol.*, *5*, 487–503.

Kao, S.-C., and R. S. Govindaraju (2007), A bivariate frequency analysis of extreme rainfall with implications for design, *J. Geophys. Res.*, *112*, D13119, doi:10.1029/2007JD008522.

Kao, S.-C., and R. S. Govindaraju (2008), Trivariate statistical analysis of extreme rainfall events via the Plackett family of copulas, *Water Resour. Res.*, *44*, W02415, doi:10.1029/2007WR006261.

Kidd, C., V. Levizzani, and S. Laviola (2010), Quantitative precipitation estimation from Earth observation satellites, in *Rainfall: State of the Science*, *Geophys. Monogr. Ser.*, doi: 10.1029/2009GM000920, this volume.

Krajewski, W. F., and J. A. Smith (2002), Radar hydrology: Rainfall estimation, *Adv. Water Resour.*, *25*, 1387–1394.

Krajewski, W. F., G. Villarini, and J. A. Smith (2010), Radar-rainfall uncertainties: Where are we after thirty years of effort?, *Bull. Am. Meteorol. Soc.*, *91*, 87–94.

Laws, J. O. (1941), Measurements of the fall-velocity of water-drops and rain drops, *Eos Trans. AGU*, *22*, 709–721.

List, R., and G. M. McFarquhar (1990), The evolution of three-peak raindrop size distributions in one-dimensional shaft models. Part I: Single-pulse rain, *J. Atmos. Sci.*, *47*(24), 2996–3006.

List, R., N. R. Donaldson, and R. E. Stewart (1987), Temporal evolution of drop spectra to collisional equilibrium in steady and pulsating rain, *J. Atmos. Sci.*, *44*(2), 362–372.

Low, T. B., and R. List (1982a), Collision, coalescence and breakup of raindrops. Part I: Experimentally established coalescence efficiencies and fragment size distributions in breakup, *J. Atmos. Sci.*, *39*(7), 1591–1606.

Low, T. B., and R. List (1982b), Collision, coalescence and breakup of raindrops. Part II: Parameterization of fragment size distributions, *J. Atmos. Sci.*, *39*(7), 1607–1618.

Mandapaka, P. V., and U. Germann (2010), Radar-rainfall error models and ensemble generators, in *Rainfall: State of the Science*, *Geophys. Monogr. Ser.*, doi:10.1029/2010GM001003, this volume.

Marshall, J. S., and W. McK. Palmer (1948), The distribution of raindrops with size, *J. Meteorol.*, *5*, 165–166.

Mason, B. J. (1971), *The Physics of Clouds*, Clarendon, Oxford, U. K.

McDonald, J. E. (1954), The shape and aerodynamics of large raindrops, *J. Meteorol.*, *11*, 478–494.

McFarquhar, G. M. (2004), A new representation of collision-induced breakup of raindrops and its implications for the shapes of raindrop size distributions, *J. Atmos. Sci.*, *61*(7), 777–794.

McFarquhar, G. M. (2010), Raindrop size distribution and evolution, in *Rainfall: State of the Science*, *Geophys. Monogr. Ser.*, doi:10.1029/2010GM000971, this volume.

Mircea, M., S. Stefan, and S. Fuzzi (2000), Precipitation scavenging coefficient: Influence of measured aerosol and raindrop size distributions, *Atmos. Environ.*, *34*, 5169–5174.

Panagopoulos, A. D., and J. D. Kanellopoulos (2002), Adjacent satellite interference effects as applied to the outage performance of an Earth-space system located in a heavy rain climatic region, *Ann. Telecommun.*, *57*(9–10), 925–942.

Pruppacher, H. R., and J. D. Klett (1978), *Microphysics of Clouds and Precipitation*, Kluwer, Dordrecht, Netherlands.

Pruppacher, H. R., and R. L. Pitter (1971), A semi-empirical determination of the shape of cloud and rain drops, *J. Atmos. Sci.*, *28*(1), 86–94.

Rogers, R. R., and M. K. Yau (1989), *A Short Course in Cloud Physics*, Pergamon, New York.

Salvadori, G., and C. De Michele (2004a), Analytical calculation of storm volume statistics involving Pareto-like intensity–duration marginals, *Geophys. Res. Lett.*, *31*, L04502, doi:10.1029/2003GL018767.

Salvadori, G., and C. De Michele (2004b), Frequency analysis via copulas: Theoretical aspects and applications to hydrological events, *Water Resour. Res.*, *40*, W12511, doi:10.1029/2004WR003133.

Sapiano, M. R. P., J. E. Janowiak, W. Shi, R. W. Higgins, and V. B. S. Silva (2010), Regional evaluation through independent precipitation measurements: USA, in *Satellite Rainfall Applications for*

Surface Hydrology, edited by M. Gebremichael and F. Hossain, pp. 169–192, doi:10.1007/978-90-481-2915-7_10, Springer, New York.

Savic, P. (1953), Circulation and distortion of liquid drops falling through a viscous medium, *Rep. NRC-MT-22*, 50 pp., Natl. Res. Counc., Ottawa, Ont., Canada.

Scofield, R. A., and R. J. Kuligowski (2003), Status and outlook of operational satellite precipitation algorithms for extreme-precipitation events, *Weather Forecasting*, *18*, 1037–1051.

Seo, D.-J., A. Seed, and G. Delrieu (2010), Radar and multisensor rainfall estimation for hydrologic applications, in *Rainfall: State of the Science*, *Geophys. Monogr. Ser.*, doi:10.1029/2010GM000952, this volume.

Sharma, A., and R. Mehrotra (2010), Rainfall generation, in *Rainfall: State of the Science*, *Geophys. Monogr. Ser.*, doi:10.1029/2010GM000973, this volume.

Sklar, A. W. (1959), Fonctions de répartition à n dimension et leurs marges, *Publ. Inst. Stat. Univ. Paris*, *8*, 229–231.

Sorooshian, S., K. Hsu, X. Gao, H. V. Gupta, B. Imam, and D. Braithwaite (2000), Evaluation of PERSIANN system satellite-based estimates of tropical rainfall, *Bull. Am. Meteorol. Soc.*, *81*, 2035–2046.

Spilhaus, A. F. (1948), Raindrop size, shape, and falling speed, *J. Meteorol.*, *5*, 108–110.

Tian, Y., C. D. Peters-Lidard, B. J. Chaudhury, and M. Garcia (2007), Multitemporal analysis of TRMM-based satellite precipitation products for land data assimilation applications, *J. Hydrometeorol.*, *8*, 1165–1183.

Turk, F. J., and S. Miller (2005), Toward improving estimates of remotely-sensed precipitation with MODIS/AMSR-E blended data techniques, *IEEE Trans. Geosci. Remote Sens.*, *43*, 1059–1069.

Ushio, T., and M. Kachi (2010), Kalman filtering applications for global satellite mapping of precipitation (GSMaP), in *Satellite Rainfall Applications for Surface Hydrology*, edited by M. Gebremichael and F. Hossain, pp. 105–123, doi:10.1007/978-90-481-2915-7_7, Springer, New York.

Valdez, M. P., and K. C. Young (1985), Number fluxes in equilibrium raindrop populations: A Markov chain analysis, *J. Atmos. Sci.*, *42*(10), 1024–1036.

Wang, P. K., and H. R. Pruppacher (1977), Acceleration to terminal velocity of cloud and raindrops, *J. Appl. Meteorol.*, *16*, 276–280.

Wang, X., M. Gebremichael, and J. Yan (2010), Weighted likelihood copula modeling of extreme rainfall events in Connecticut, *J. Hydrol.*, *230*, 108–115.

Wilson, J. W., and E. A. Brandes (1979), Radar measurement of rainfall–A summary, *Bull. Am. Meteorol. Soc.*, *60*, 1048–1058.

Zawadzki, I. (1982), The quantitative interpretation of weather radar measurements, *Atmos. Ocean*, *20*, 158–180.

Zhang, L., and V. P. Singh (2007), Bivariate rainfall frequency distributions using Archimedean copulas, *J. Hydrol.*, *332*(1–2), 93–109.

M. Gebremichael, Department of Civil and Environmental Engineering, University of Connecticut, Storrs, CT 06269-2037, USA.

F. Y. Testik, Department of Civil Engineering, Clemson University, Clemson, SC 29634, USA. (ftestik@clemson.edu)

Raindrop Morphodynamics

B. K. Jones

Department of Mechanical Engineering, Columbia University, New York, New York, USA

J. R. Saylor

Department of Mechanical Engineering, Clemson University, Clemson, South Carolina, USA

F. Y. Testik

Department of Civil Engineering, Clemson University, Clemson, South Carolina, USA

In the absence of forces other than surface tension, a water drop will attain a perfectly spherical shape. Raindrops experience a range of forces, including those due to fluid flow (both inside and outside the drop), hydrostatic forces, and electrostatic forces. A falling raindrop deviates in shape from spherical, becoming a flattened oblate spheroid, a shape that becomes more prominent as the raindrop diameter increases. This shape is characterized by a chord ratio, which is the ratio of the height to the width of the raindrop. The drop shape is often variable, oscillating because of excitation of the natural frequencies of the drop by the flow of fluid around the drop and through interactions between the natural frequency of the drop and vortex shedding in the wake of the drop. These interactions make raindrop morphodynamics, the study of the dynamic and stable raindrop shape, an especially rich problem. Drop collisions also affect the transient behavior of drop shape. Polarimetric radar techniques have further motivated studies of raindrop morphodynamics, since knowledge of raindrop shape can be utilized to improve rain rate retrievals using these radars. Experimentation and analytical efforts have explored several facets of raindrop morphodynamical behavior, including raindrop fall speeds, nonoscillating and oscillating shapes, chord ratio versus diameter relationships, oscillation frequencies, and the preferred harmonic modes, for example. Herein, we provide a survey of the current state of knowledge of these aspects of raindrop morphodynamics.

1. INTRODUCTION

As water vapor in the atmosphere condenses, liquid droplets are initially sufficiently small to remain aloft, entrained in air currents. The motion of these cloud droplets causes them to collide with one another and form either permanent unions or smaller fragment droplets. In this manner, some drops increase in mass until the force of gravity exceeds the momentum available from the air motion, and they begin to fall. This collision and fragmentation occurs in falling drops as well. In fact, an upper size limit is determined as some falling drops coalesce until breakup invariably occurs due to hydrodynamic instability [*Pruppacher and*

Rainfall: State of the Science
Geophysical Monograph Series 191

10.1029/2009GM000928

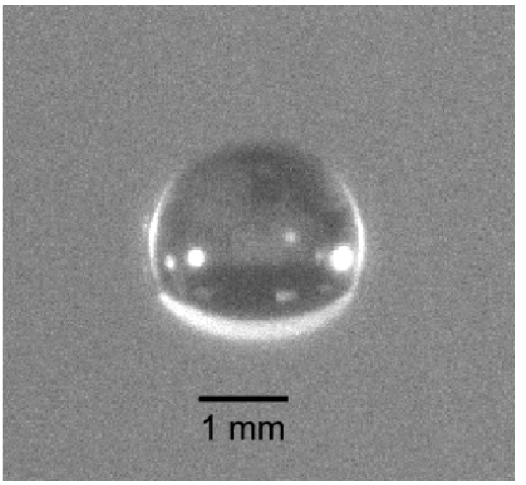

Figure 1. Water drop levitated in a vertical wind tunnel illustrating the characteristic shape of a quiescent raindrop.

Pitter, 1971] or because of drop-drop collision. If they remain in the liquid phase, these hydrometeors are referred to as raindrops. Due to their fluid nature, raindrops assume a variety of complex shapes and shape-altering oscillations during free fall. The study of this static and dynamic behavior is referred to as raindrop "morphodynamics" and is based primarily in fluid mechanics. The characteristic shape of a nonoscillating (hereafter "equilibrium") raindrop is shown in Figure 1.

Voluminous work involving a variety of theoretical modeling and experimentation can be found on this subject in the literature (see *Testik and Barros* [2007] for an extensive review). Experimenters have utilized high-speed photography of natural rain [*Testik et al.*, 2006], for example, or devised creative methods to elucidate real raindrop behavior from water drops floating in wind tunnels [*Beard and Pruppacher*, 1969; *Pruppacher and Beard*, 1970; *Kamra et al.*, 1986; *Saylor and Jones*, 2005; *Szakall et al.*, 2009; *Jones and Saylor*, 2009] or falling from high stairwells, towers, or highway bridges [*Andsager et al.*, 1999; *Thurai and Bringi*, 2005]. Theoretical models of raindrop shape reflect the solution of complex differential equations that rely on prior empirical observations for boundary conditions and validation. The accuracy of these calculated shapes, when compared with observations of real raindrops, has chronologically increased as researchers have improved upon the assumptions, techniques, and errors of their predecessors.

Aside from scientific novelty, the study of raindrop morphodynamics is an important aspect of precipitation science, global hydrology, weather radar science [*Chandrasekar et al.*, 2008], and satellite and terrestrial communication techniques [*Thurai and Bringi*, 2005]. For example, accurate evaluation of dual-polarization (also "polarimetric") weather radar relies upon precise knowledge of raindrop shapes. Raindrops can also attenuate and disrupt wireless communication links operating at or above microwave frequencies, so correcting for these errors may be possible with more advanced knowledge of raindrop morphodynamic behavior [*Allnutt*, 1989].

The remainder of this chapter encompasses six sections. A brief background on the fluid dynamics of raindrops is provided in section 2. The equilibrium raindrop shape is introduced in section 3. Raindrop oscillations and resulting shape changes are discussed in section 4. The effect of raindrop shape on terminal fall velocity u_t is presented in section 5, and in section 6, the effect of electrical fields on raindrop shape is discussed. Experimental techniques used to study raindrops are presented in section 7.

2. BACKGROUND ON RAINDROP FLUID DYNAMICS

The airflow past a raindrop and the water flow inside a raindrop in free fall are governed by the continuity equation and the Navier-Stokes equations of motion, subject to the appropriate boundary conditions. However, being a nonlinear system of coupled partial differential equations, analytical solution of the Navier-Stokes equations is currently prohibitively complex unless simplifications can be introduced. Discussion of the Navier-Stokes equations and their theoretical treatment in the context of raindrops is given by *Pruppacher and Klett* [1997] and is not presented here. Further discussion of flows relevant to raindrops can be found in various graduate-level fluid mechanics textbooks [e.g., *Batchelor*, 1967; *Landau and Lifshitz*, 1959].

There are primarily three dimensionless parameters pertinent to the morphodynamics of raindrops in free fall: the Reynolds number *Re*, Weber number *We*, and Strouhal number *St*, defined as

$$Re = Ud/\nu, \tag{1}$$

$$We = \rho_a U^2 d/\sigma, \tag{2}$$

$$St = f_w d/U, \tag{3}$$

where U is the relative velocity (fall speed) between the airstream and the raindrop during free fall, d is the raindrop diameter, ν and ρ_a are the kinematic viscosity and density of air, respectively, σ is the surface tension of water, and f_w is the frequency of vortex shedding in the drop wake, relevant to larger raindrops (discussed below). Because of the variable

Table 1. Approximate Values of *Re* and *We* as a Function of Drop Diameter *d* for Raindrops

d (mm)	*Re*	*We*
0.2	10	$8.6(10^{-4})$
1.0	400	0.3
2.0	1380	1.4
3.0	2510	3.1
4.0	3670	5.0
5.0	4810	6.8
6.0	5920	8.6

nature of raindrop shape, the drop diameter *d* refers to the diameter of an equivalent volume sphere. The variation in morphodynamic behavior that raindrops exhibit can be correlated to these dimensionless parameters, since the ratios in equations (1)–(3) represent the relative magnitudes of underlying fluid forces. Specifically, *Re* is the ratio of inertial to viscous forces, while *We* is the ratio of inertial to surface tension forces. The Strouhal number *St* is the dimensionless frequency of periodic behavior in the raindrop wake, which arises for $d > 1$ mm. Based on similarity arguments [see, e.g., *Barenblatt*, 2003], by matching these parameters in fluid systems other than air/water, inferences can be made regarding raindrop behavior, an approach which can simplify experimentation (see below).

Because a drop of given diameter has a nominally fixed maximum (terminal) fall velocity (see section 5) (u_t, U in equations (1) and (2)) is a function of *d*. Hence, *Re* and *We* are essentially determined by *d*, except after drop collisions when U is readjusting to u_t. The values that *Re* and *We* attain at u_t for a span of *d* representative of raindrops is presented in Table 1, showing that the range of *Re* and *We* for raindrops spans nearly four orders of magnitude, an indication of the widely varying balance of forces.

The characteristics of the airflow around a falling raindrop vary significantly with *d* and thus fall speed and the governing dimensionless parameters. Laboratory visualizations of freely falling drops suggest that for raindrops with $Re \gtrsim 210$–270, a separated wake develops in the downstream region of the drop [*Margarvey and Bishop*, 1961]. The presence of this wake region alters the pressure distribution around the raindrop, inducing static and dynamic changes in the raindrop shape. Direct observation of this coupling between shape and wake behavior is a significant experimental challenge, and analogous fluid systems have been studied to elucidate the nature of the relationship for raindrops. For example, *Magarvey and MacLatchy* [1965] described the wakes of solid spheres falling through a liquid bulk, a fluid system which deviates from the raindrop case due to the rigidity of the sphere surface; for liquid drops, the deforming surface is a significant dissipator of energy. While these deviations somewhat complicate an exact comparison with raindrops, on the other hand, rigid sphere studies facilitate isolation of the wake formation mechanisms from the effects of the liquid drop free surface.

For solid spheres at $Re = 1$–200, *Magarvey and MacLatchy* [1965] reported a steady vortex trail in which vorticity is convected directly to the freestream. At $Re = 200$–300, an axisymmetric (refers to symmetry about the drop fall axis) near-wake develops immediately downstream of the sphere. This increasing vorticity is first dissipated by circulation within the wake, then convected to the freestream in two parallel vortex trails. Asymmetry develops in the range $Re = 300$–450, as the volume of the near-wake periodically varies at fixed *Re* in the following manner. With each circulation of the wake region, increasing amounts of freestream fluid are entrained until a portion of the near-wake detaches, forming an eddy that sheds downstream. The general pattern of this process is shown in Figure 2. Initially, at $Re \approx 300$, eddies detach from only one side of the sphere, but with increasing *Re*, they begin to detach from opposite sides similar to the Karman vortex street. For fixed *Re*, the periodicity of this process reaches a steady state and gives rise to an oscillatory wake, characterized by the Strouhal number *St* (equation (3)).

Margarvey and Bishop [1961] classified the wakes of dyed liquid drops falling in a liquid bulk at *Re* similar to raindrops falling at u_t and found the distinct regimes outlined in Table 2. This work is more detailed than the solid sphere observations reported by *Magarvey and MacLatchy* [1965] described above. They also described a steady, axisymmetric wake developing at $Re \approx 20$, appearing as a single thread downstream of the drop. This structure prevails for $d \leq$

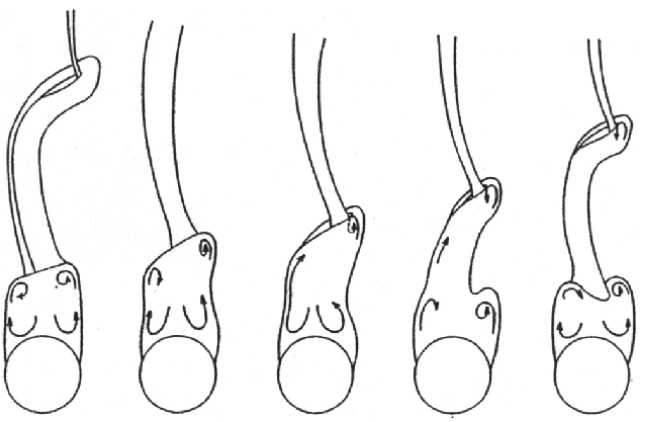

Figure 2. Temporal evolution (from left to right) of vortex shedding pattern in the wake of a solid sphere at $Re < 800$, as illustrated by *Sakamoto and Haniu* [1990]. From *Sakamoto and Haniu* [1990]. Copyright ASME.

Table 2. Classification of Wakes of Freely Falling Liquid Drops and Spheres[a]

Class	*Re* Range	*d* (mm)	Description of Wake
I	0–210	<0.9	Steady single thread
II	210–270	0.9–1.0	Asymmetric double thread
III	270–290	1.0–1.1	Double thread with waves
IV	290–410	1.1–1.3	Double row of vortex loops
V	290–700	1.1–1.8	Double row of vortex rings
VI	700–2500	1.8–4.2	Irregular vortex pattern

[a]The size (*d*) is given for raindrops falling in air. Class IV and V wakes simultaneously exist in the range *Re* = 290–410.

0.9 mm drops. With increasing *Re* and *d*, the circulating near-wake region grows until the vorticity generated can no longer be dissipated in this symmetric manner. Consequently, at $d \approx$ 0.9 mm, the point of detachment suddenly migrates from the fall axis to one side of the drop, and a double-threaded wake develops. The resulting lateral force on the drop produces a sideways drift, in agreement with the observations of *Gunn* [1949] describing the sideways and spiraling free fall of similar-sized drops in calm air, and the solid sphere observations of *Magarvey and MacLatchy* [1965]. At d = 1.0 mm, periodicity initiates at *Re* = 270 as the double-thread begins to oscillate. With further increases in *Re*, vortex loops and rings develop as outlined above and in Table 2, with the concomitant spiraling free fall seemingly caused by the precession of wake detachment points, also described by *Magarvey and MacLatchy* [1965].

3. DROP SHAPE

The shape of a falling raindrop is determined by the mechanical equilibrium of the liquid-gas interface defining its outer surface. During free fall, an aerodynamic pressure difference arises between the upper and lower poles and the equator of the raindrop, in addition to an internal circulation because of the no-slip boundary condition at the drop surface. The resulting forces, together with electrostatic forces, internal hydrostatic pressure and surface tension, balance to produce an equilibrium shape resembling a flattened sphere with a wide horizontal base and a smoothly curved upper surface. This shape varies with *d*, consequently small drops are essentially spherical while larger drops are more distorted. Figure 3 shows this effect, best characterized by the variation in the raindrop chord axis ratio, defined as the ratio of the vertical extent *a* to the horizontal extent *b* of the drop, or

$$\alpha = a/b. \tag{4}$$

Because of this flattening of raindrop shape with size, the ratio α decreases with increasing *d*. This trend persists until

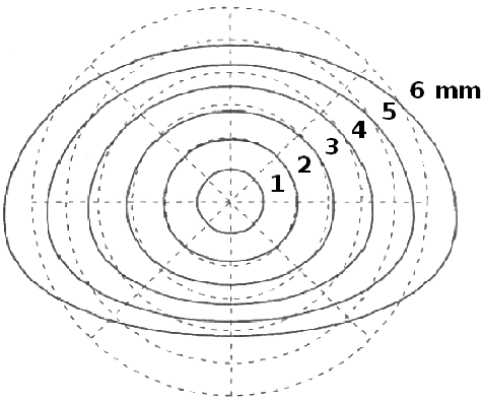

Figure 3. Calculated raindrop shapes from the numerical model due to *Beard and Chuang* [1987]. From *Beard and Chuang* [1987]. Copyright 1987 American Meteorological Society.

fragmentation occurs, typically around $d \approx$ 6–8 mm [*Pruppacher and Pitter*, 1971], although extraordinary instances of *d* larger than 8.8 mm [*Hobbs and Rangno*, 2004] and 10 mm [*Takahashi et al.*, 1995] have been observed in tropical clouds.

This predictable variation of α with *d* is the key principle behind polarimetric radar techniques [*Seliga and Bringi*, 1976]. Measurement of rain rate *R* using traditional single-polarization radar involves transmitting a microwave signal and measuring the intensity of the echo backscattered by raindrops. This intensity determines a reflectivity factor *Z*, which is used to estimate parameters of the drop size distribution. If the Rayleigh approximation is made for the backscattering cross-section of raindrops, the reflectivity factor *Z* and *R* are related to this drop size distribution by [*Doviak and Zrnić*, 1984]

$$Z = \int_0^\infty N(D) D^6 dD \tag{5}$$

$$R = \frac{\pi}{6} \int_0^\infty D^3 N(D) u_t(D) dD, \tag{6}$$

where $N(D)$ is the drop size distribution (DSD), u_t is the terminal velocity, and D is the drop diameter (equivalent to d).

The DSD is typically modeled as the Marshall-Palmer spectrum

$$N(D) = N_0 e^{-\Lambda D}, \tag{7}$$

having two parameters Λ and N_0. Substituting equation (7) into equation (5) yields, after integration,

$$Z = N_0 (6!) \Lambda^{-7}. \tag{8}$$

Equation (8) reveals the primary obstacle to using single-polarization radar for the measurement of R: how to determine the two unknown parameters Λ and N_0 from the single measurement Z? The solution is to utilize dual-polarization radars. Because of the importance of drop shape to this measurement method, we now describe how dual-polarization radar measurement of rain is implemented.

In the most common implementation of this technique, the transmitted radar signal is repeatedly switched between a horizontal and vertical polarization so that two reflectivity factors, Z_H and Z_V, are measured by the receiver. The ratio of these factors gives the differential reflectivity Z_{DR}, defined as

$$Z_{DR} = 10\log(Z_H/Z_V) \quad (\text{dB}). \tag{9}$$

This differential reflectivity varies with the specific drop sizes that are aloft during sensing, since different-sized drops exhibit distinctly different α values as shown in Figure 3. Following the treatment of *Ulbrich* [1986], R is related to Z_{DR} by equation (9) and the definitions of Z_H and Z_V, given by

$$Z_{H,V} = \frac{10^6\lambda^4}{\pi^5 K^2}\int_{D_{\min}}^{D_{\max}} \sigma_{H,V}(D)N(D)dD, \tag{10}$$

where $\sigma_{H,V}$ is [*Gans*, 1912]

$$\sigma_{H,V} = \frac{16\pi^7 D^6}{9\lambda^4}\left|\frac{\eta^2-1}{4\pi+(\eta^2-1)P_{H,V}}\right|^2 \tag{11}$$

$$P_V = \frac{4\pi}{e^2}\left[1-\sqrt{(1-e^2)/e^2}\sin^{-1}e\right] = 4\pi - 2P_H. \tag{12}$$

Here λ is the radar signal wavelength, $|K|^2 = 0.93$ is the dielectric factor for water, η is the complex refractive index of water, and e is the drop eccentricity related directly to α by

$$e^2 = 1-\alpha^2. \tag{13}$$

Estimates of R are obtained from measurements of Z_{DR} by determining N_0 and Λ (or the median volume diameter D_0, where $D_0 = 3.672/\Lambda$ after *Ulbrich* [1986]), which are then used in equations (6) and (7). Note that the parameter N_0 falls out of equation (9), since it is a constant that appears in the integrand for both Z_H and Z_V. Hence, by obtaining plots of Z_{DR} versus D_0 (viz. versus Λ) using the equations developed above, one can convert a measured Z_{DR} to a value of Λ after appropriate assumptions regarding the maximum and minimum drop sizes $D_{\max}$, $D_{\min}$ aloft during the rain event. Measurements of Z_H are then used along with this value in equation (10) to find N_0, which enters this equation in $N(D)$ (see equation (7)). This entire method is predicated on the variation of α with d, which enters into the retrieval of R in equation (13) and propagates through the other equations. This shows the critical nature of the α versus d relationship in the use of dual-polarization radar measurements of R [*Bringi and Chandrasekar*, 2001; *Goddard et al.*, 1994a].

Based upon laboratory observations, *Pruppacher and Pitter* [1971] described the variation with d of raindrop shapes as a continuum with three distinct diameter ranges: Class I ($d <$ 0.25 mm), Class II (0.25 mm $\le d \le$ 1 mm), and Class III ($d >$ 1 mm). Specifically, Class I drops exhibit no detectable distortion from sphericity. These shapes are dominated by surface tension, which effectively minimizes the energy and surface area of the drop, requiring a spherical shape. Class II drops exhibit a slight distortion with a discernible increase in radius of curvature of the lower hemisphere, a shape termed "oblate spheroidal." Class III category drops show further, marked distortion with increasing diameter, the oblate spheroid shapes exhibiting an increased flattening of the lower surface corresponding to a reduction in axis ratio. These observations are summarized in Table 3.

Early work on the development of a mathematical relationship between α and d focused on confirming and clarifying the relative roles of five physical factors: (1) surface tension, which forces a more spherical shape; (2) internal hydrostatic pressure, a vertical pressure gradient within the drop, acting outward against surface tension; (3) external aerodynamic pressure, which flattens the raindrop as it creates an increase in air pressure at the base and a decrement elsewhere; (4) internal circulation, which creates a toroidal-vortex flow within the drop, inducing complex effects on shape; and (5) electrostatic forces that may accentuate or suppress oblateness depending on drop electrical charge and field conditions [*Lenard*, 1904; *McDonald*, 1954a]. The dominance of the first three factors has been established; however, the role of internal circulation and electrostatic forces in controlling drop shape has yet to be fully understood [*Testik and Barros*, 2007]. This is because reported results on the amplitudes of internal circulation in raindrops falling at terminal velocity are rather contradictory [*Blanchard*, 1949; *McDonald*, 1954a; *Garner and Lane*, 1959; *Foote*, 1969; *Pruppacher and Beard*, 1970]. Additionally, electrostatic forces may have a strong, nonlinear effect on drop distortion in certain thunderstorm conditions [*Beard et al.*, 1989a; *Bhalwankar and Kamra*, 2007; *Beard et al.*, 2004].

Table 3. Classification of Drop Distortion With Size (d)

Class	d (mm)	Drop Shape
I	<0.25	No detectable distortion
II	0.25–1.0	Slightly aspherical
III	>1.0	Markedly oblate spheroidal

Two theoretical approaches have been used in raindrop shape models: "gravity" models and "perturbation" models. Gravity models derive an α versus d relationship from a balance of gravity and surface energy [*Beard*, 1984a], or surface tension and either external or internal pressure [*Green*, 1975; *Spilhaus*, 1948], often attaining considerable accuracy despite their relative simplicity. By comparison, the more rigorous perturbation models [*Imai*, 1950; *Savic*, 1953; *Pruppacher and Pitter*, 1971] utilize Laplace's pressure balance, which relates the curvature at each point on the drop surface to the internal and external pressures by

$$\sigma\left[\frac{1}{R_1}+\frac{1}{R_2}\right]=\Delta p, \tag{14}$$

where R_1 and R_2 give the radii of curvature, and Δp gives the pressure difference across the drop surface (for derivation, see *Landau and Lifshitz* [1959]). The system of differential equations in equation (14) describes the complete drop silhouette. Typically, solutions to this system of equations are obtained numerically and incorporate empirical pressure measurements from wind tunnel data, a method first proposed by *Savic* [1953]. Pressure measurements from rigid spheres were used by *Pruppacher and Pitter* [1971] and others until more recently, when the technique was adapted by *Beard and Chuang* [1987] to account for an altered pressure field from drop distortions.

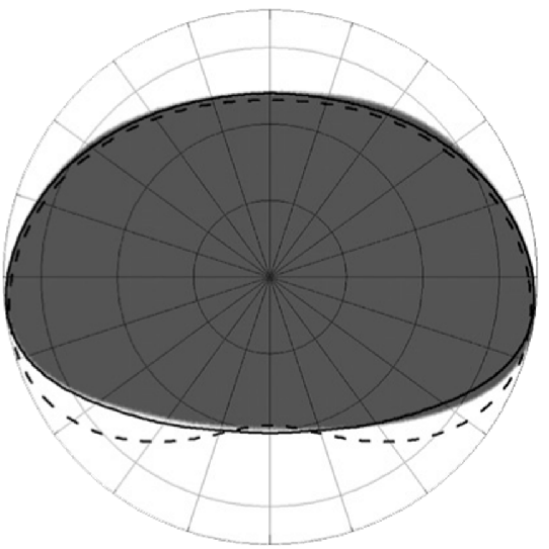

Figure 4. Comparison of the *Beard and Chuang* [1987] raindrop shape model (solid line) with the silhouette of a 6-mm wind tunnel drop (shadow) and the model of *Pruppacher and Pitter* [1971] (dashed line). From *Szakall et al.* [2009]. Copyright 2009 American Meteorological Society.

Their model, which compares well with field [*Chandrasekar et al.*, 1988; *Bringi et al.*, 1998] and laboratory [*Szakall et al.*, 2009; *Thurai et al.*, 2007] observations, is widely accepted as the most realistic for determining raindrop equilibrium shapes. A recent validation by *Szakall et al.* [2009] is shown in Figure 4.

4. DROP OSCILLATION

Schmidt [1913] was the first to observe oscillations in the shape of raindrops, and it is well known that $d \geq 1$ mm (Class III) drops may oscillate during free fall so that their shapes vary about the equilibrium shape [*Gunn*, 1949; *Jones*, 1959]. This complicates the α versus d relationship because instantaneous α measurements often scatter widely. Hence, the accurate interpretation of radar backscatter from oscillating drops requires precise knowledge of the "time-average" (mean) axis ratio as a function of drop diameter. Considerable research has been conducted to elucidate this behavior. Figure 5 shows a sequence of superposed images of a single oscillating drop, with the instants of maximum and minimum amplitude shown approximately at c and h, and f and j, respectively.

Rayleigh [1879] showed that drop oscillations occur at n discrete harmonics and with frequency f decreasing with d according to

$$f=[2n(n-1)(n+2)\sigma]^{1/2}[\pi^2\rho d^3]^{-1/2}, \tag{15}$$

where ρ gives the bulk density of water. Rayleigh's solution assumes only axisymmetric motion of a spherical, inviscid drop oscillating with small amplitude ($A << r_0$, where A is the amplitude of drop oscillation, and r_0 is the unperturbed radius of the spherical drop); *Landau and Lifshitz* [1959] further generalized the problem and found that for each n harmonic frequency, there is one axisymmetric mode at m = 0 plus $m = n$ additional unique modes, differentiated hereafter by the ordered pair (n,m). The shapes are given for a spherical coordinate system by

$$r_{n,m}(t,\theta,\varphi)=r_0+A\sin\omega t P_{n,m}\cos m\varphi, \tag{16}$$

where $\omega = 2\pi f$, and $P_{n,m}$ are the associated Legendre functions (see Appendix B). These oscillation modes are illustrated in Figure 6 superimposed on a sphere for the fundamental (n = 2) and first (n = 3) harmonic, the two deemed most realistic due to an incompressibility constraint for $n < 2$ and the role of viscous damping in diminishing the amplitudes of higher modes. It should be noted that while equation (15) gives the oscillation frequency as a function of n and d alone, calculations and empirical data show that the

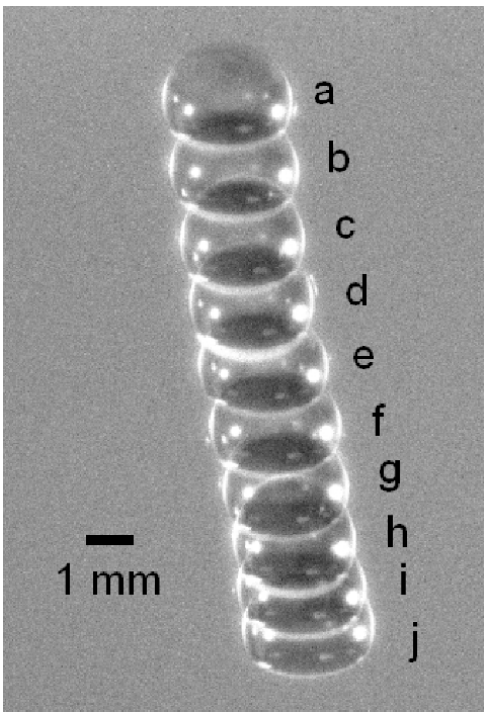

Figure 5. Superposed images of a single oscillating water drop slowly rising in the test section of a vertical wind tunnel ($d \approx 2.3$ mm, frame rate = 109 Hz).

frequency changes with mode m when the quiescent shape is distorted (i.e., nonspherical).

Observations of oscillating drops often reveal the higher-amplitude, simpler shapes of the fundamental more than the first harmonic. However, multiple modes may exist simultaneously. Moreover, modal preferences at a particular d seem to vary widely. From wind tunnel experiments, *Blanchard* [1948, 1950] reported observations of the fundamental axisymmetric (2,0) and fundamental horizontal (2,2) modes for large drops (d = 6–9 mm). *Brook and Latham* [1968] and *Nelson and Gokhale* [1972] later described purely axisymmetric oscillations for d = 3.7–5.6 mm and d = 1–3 mm drops, respectively. However, *Nelson and Gokhale* [1972] noted the presence of additional modes for d = 4–7 mm drops, and *Beard* [1984b] observed evidence of the fundamental transverse (2,1) mode in the photographs of *Nelson and Gokhale* [1972] and *Musgrove and Brook* [1975]. These laboratory observations and the field results of *Jones* [1959] show a characteristic scatter in both instantaneous and mean α.

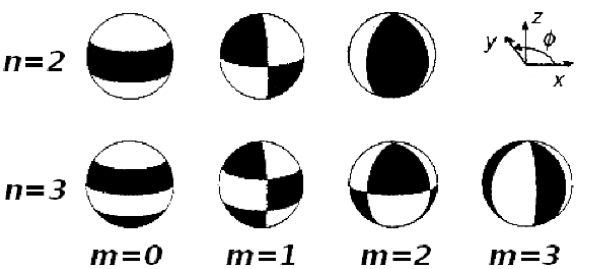

Figure 6. Orientation of perturbations given by spherical harmonic theory (equation (16)) for the fundamental (n = 2) and first (n = 3) harmonic. From *Beard and Kubesh* [1991]. Copyright 1991 American Meteorological Society.

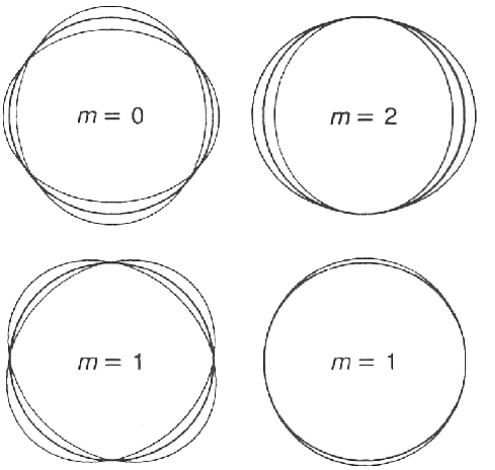

Figure 7. Views of the fundamental spherical harmonic (2,m). Two views of the fundamental transverse mode are shown, illustrating the dependence of α on the orientation ϕ of the drop. From *Beard et al.* [1989b]. Reprinted by permission from Macmillan Publishers Ltd. Copyright 1989.

Beard and Kubesh [1991] examined the theoretical shapes shown in Figure 6 and identified the specific α variation for each mode. They determined that the transverse (2,1) mode gives a strictly positive variation in α toward unity. For this mode, the drop chords exhibit two variances, depending on the viewing angle ϕ: either together, giving no change in α (see bottom-left sketch in Figure 7), or independently with b remaining static and a varying positively (bottom-right sketch of Figure 7). In contrast, axisymmetric oscillations always produce a two-sided variation because both a and b vary in an opposing manner, independent of viewing angle. The horizontal mode (see top-right sketch in Figure 7) similarly produces a two-sided variation because of static a for this mode. Thus, with respect to the equilibrium α, the mean α of an oscillating drop may or may not shift, depending on the prevailing mode. As such, modal behavior can be inferred from the scatter and mean of α measurements of oscillating drops.

Because the shift can be significant and varying, a precise formulation of mean α versus d for radar and microwave scattering applications is important. *Seliga and Bringi* [1976]

found polarimetric radar signals altered by 30% because of uncertainty in mean α, leading to erroneous estimates of drop size and rainfall rate [*Kubesh and Beard*, 1993].

Although the pioneering work of *Rayleigh* [1879] neglected any consideration of viscosity, *Lamb* [1881] showed that for small viscosity ($\nu/\omega r_0^2 << 1$, where $\omega = 2\pi f$), the main effects were a reduction in the oscillation amplitude, with higher-order modes dampening more quickly than the fundamental modes. Following this early work, most theoretical oscillation models [*Lamb*, 1932; *Foote*, 1973; *Tsamopoulos and Brown*, 1983; *Naterajan and Brown*, 1987] were based upon a spherical equilibrium shape in the absence of external fields. *Foote* [1973] introduced the first numerical model to study drop oscillations. This model used the finite-difference method to integrate the incompressible form of the Navier-Stokes equations, with surface tension effects incorporated through the use of Laplace's pressure balance (equation (14)) to define the drop surface curvature.

In an early work on the causes of oscillations, *Beard* [1984a] modeled the axisymmetric and horizontal mode for an ellipsoidal drop using a potential energy function that accounted for surface and energy due to gravity. Calculations of mean α, determined by assuming a steady state governed by a balance of collisional energy and viscous dissipation, showed a shift from equilibrium for larger drops ($d \geq 3$ mm), indicating the significant effect of collision-induced oscillations to an extent that increased with rainfall rate. *Beard* [1984b] compared this potential energy model to the available theory and found good agreement with the numerical result due to *Foote* [1973] with respect to time-varying α behavior. However, frequency calculations from this potential energy model compared more closely with experimental observations of the horizontal mode than with the axisymmetric mode, an error *Beard* [1984b] attributed to an inappropriate assumption regarding gravitational energy.

Feng and Beard [1991] described a rigorous multiple-parameter perturbation method that determined the characteristic frequencies for the specific fundamental modes ($n = 2$, $m = 0,1,2$). This eliminated the degeneracy whereby previously the spherical modes all had the same frequency (i.e., m independent; note the m-independence of equation (15)). The m-dependent equation they give,

$$f_{nm} = \frac{\omega_{nm}}{2\pi}\left(\frac{\sigma}{\rho r_0^3}\right)^{1/2}\left(1 - \frac{A_0^{\langle 2,1\rangle}(n,m)}{4\omega_{nm}^2}u_t^2\right), \qquad (17)$$

where u_t is the drop terminal velocity (see *Feng and Beard* [1991] for details), $A_0^{\langle 2,1\rangle}(n,m)(4\omega_{nm}^2)^{-1}$ has values −0.00804, 0.0241, and 0.121 for $m = 0$, 1 and 2, respectively, and

$$\omega_{nm}^2 = n(n-1)(n+2). \qquad (18)$$

Their result is shown in Figure 8 to be in considerable agreement with experimental data; specifically, the manner in which the bifurcation in the experimental data (indicative of m-dependence) aligns with their theory.

Although collisions are frequent enough in moderate to heavy rainfall to maintain oscillations for large raindrops ($d \geq 3$ mm), coupling with the unsteady drop wake is generally accepted as the primary physical mechanism for small drop oscillations [*Beard and Jameson*, 1983]. For smaller drop sizes, where collisions are more infrequent and viscous effects are more pronounced, coupling with the unsteady wake provides a sustained driving force to maintain oscillations against the time decay of viscous dissipation [*Johnson and Beard*, 1984]. First postulated by *Gunn and Kinzer* [1949], the mechanism is based on a match between vortex shedding and drop oscillation frequencies, as well as the simultaneous onset of both phenomena at $d \approx 1$ mm. The onset of oscillations at this drop diameter, combined with the diminished likelihood of collisional forcing as an oscillation mechanism for small

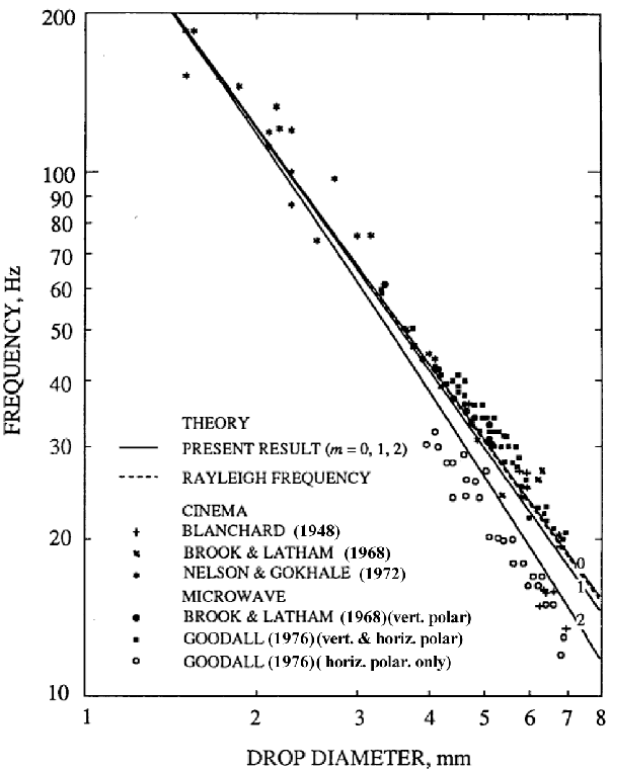

Figure 8. Oscillation frequency in Hz as a function of drop diameter in mm for the fundamental ($n = 2$) axisymmetric ($m = 0$), transverse ($m = 1$), and horizontal ($m = 2$) modes according to equation (17). Discrete points represent experimental data; lines show the m-dependent theoretical result due to *Feng and Beard* [1991]. From *Feng and Beard* [1991]. Copyright American Meteorological Society.

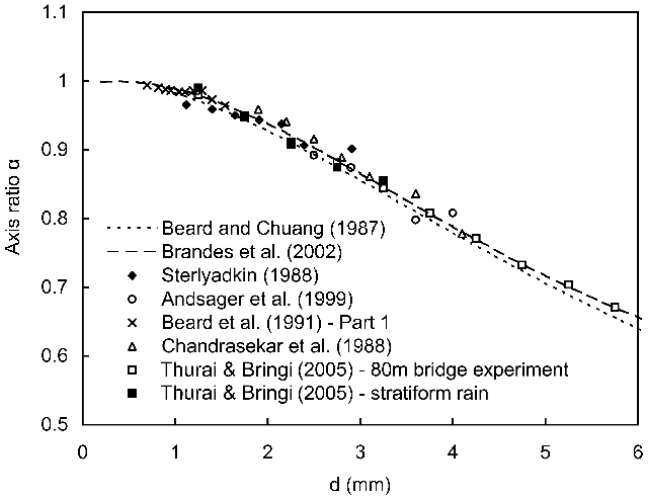

Figure 9. Empirical data for axis ratio α as a function of drop diameter d in mm, shown with the equilibrium raindrop shape model due to *Beard and Chuang* [1987] and the polynomial fit suggested by *Brandes et al.* [2002].

drop sizes, supports a causal relationship between vortex shedding and drop oscillations [*Beard and Jameson*, 1983]. With increasing d, the frequency match diverges, however, as the vortex-shedding frequency increases while the oscillation frequency decreases. Regardless, oscillations persist for larger d and increase in amplitude, as evidenced by the wide scatter in α. A transient effect reported by *Andsager et al.* [1999] suggests that the wide scatter may only occur after aerodynamic feedback reaches a steady state that is perhaps linked to eddy shedding or drag fluctuations. It is unknown exactly what resonant forcing mechanism lies behind this feedback or how and which specific oscillation modes are excited. However, the raindrop images of *Testik et al.* [2006] provide direct evidence of multimode oscillations and lateral drift. Combined with the long-speculated link between eddy shedding and lateral drift, these images suggest that the three may necessarily coexist.

A steady state combination of wake feedback, drop collisions, and turbulence seems to form the oscillation mechanism in raindrops. Because experiments have varied in their reproduction of these factors with regard to raindrop simulation, and oscillatory modal behavior has proven quite sensitive to these factors, it has been difficult to precisely characterize the mean α shift. This lack of consensus has made the determination of which α versus d relation to be used for radar calibration historically unclear. More recent work, however, seems to have identified boundaries for the mean α shift, with new data falling within range of the polynomial fits offered in the literature. A representative sampling of drop α data is presented in Figure 9. The recent data due to *Thurai and Bringi* [2005] is shown to agree reasonably well with the mean α curve due to *Brandes et al.* [2002].

A larger selection of the available α models in the literature is presented in Figure 10. Linear and nonlinear relationships are given, the former apparently being more appropriate for a particular polarimetric method of determining R [*Thurai and Bringi*, 2005] regardless of the inaccuracy due to linearization. The relationships shown in Figure 10 are summarized as follows (all units in millimeters unless specified):

1. *Pruppacher and Beard* [1970] derived a linear relationship from wind tunnel data for d = 1–9 mm, given by

$$\alpha = 1.03 - 0.062d \tag{19}$$

with d given in units of millimeters.

2. The calculated equilibrium shapes due to *Beard and Chuang* [1987] are given for d = 1–7 mm by

$$\alpha = 1.0048 + 5.7 \times 10^{-4}d - 2.628 \times 10^{-2}d^2 + 3.682 \times 10^{-3}d^3 - 1.677 \times 10^{-4}d^4, \tag{20}$$

with d given in units of millimeters.

3. *Andsager et al.* [1999] combined their data with those from *Chandrasekar et al.* [1988], *Beard et al.* [1991], and *Kubesh and Beard* [1993] to determine the following polynomial fit (in units of centimeters):

$$\alpha = 1.012 - 0.1445d - 1.03d^2, \tag{21}$$

valid for d = 1.1–4.4 mm, with equation (20) recommended for d outside this range.

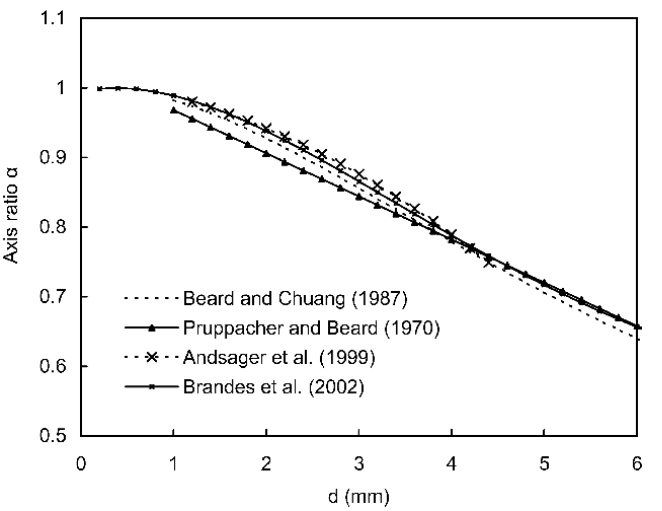

Figure 10. A selection of mean axis ratio formulations, given as a function of diameter d in mm.

4. *Brandes et al.* [2002] fit the following polynomial to the data due to *Pruppacher and Pitter* [1971], *Chandrasekar et al.* [1988], *Beard and Kubesh* [1991], and *Andsager et al.* [1999]:

$$\alpha = 0.9951 + 2.51 \times 10^{-2} d - 3.644 \times 10^{-2} d^2 + 5.303 \times 10^{-3} d^3 - 2.492 \times 10^{-4} d^4. \quad (22)$$

One method developed to address the α problem is the radar "self-consistency" principle, first described by *Gorgucci et al.* [1992], in which polarimetric radars are calibrated by calculating R from separate groups of measurables obtained by the same radar. The discrepancy arising between these R values is then correlated to raindrop shape and used to formulate an appropriate α versus d relationship. Versions of the method have been described by *Goddard et al.* [1994b], *Illingworth and Blackman* [2002], *Vivekanandan et al.* [2003], and *Ryzhkov et al.* [2005]. However, *Gourley et al.* [2009] recently utilized the method to evaluate the α models presented in Figure 10. They report minimal R error through use of either a hybrid relation consisting of equation (21) for small drops (d = 0–1.3 mm) and a formulation from *Goddard et al.* [1994b] for larger sizes (d > 1.3 mm) or equation (22).

Another method, first described by *Gorgucci et al.* [2000] and recently adapted by *Gorgucci et al.* [2008], utilizes a linear α model

$$\alpha = 1.03 - \beta d \quad (23)$$

and the self-consistency principle to optimize the variable slope parameter β (note that β = 0.062 mm^{-1} gives the *Pruppacher and Beard* [1970] α model, equation (19)). Although *Gourley et al.* [2009] determined that a similar linear model due to *Matrosov et al.* [2005] was quite sensitive to variability in α compared to a group of six other models, some radar practitioners may prefer the simultaneous DSD parameter retrieval that is a by-product of the variable β technique.

5. TERMINAL VELOCITY

The terminal velocity u_t of a raindrop is the velocity in still air achieved when the force due to gravity on the drop is exactly balanced by the (relatively small) buoyancy force and the aerodynamic drag force caused by airflow over the drop. While the aerodynamic drag increases roughly with the square of the drop diameter, the gravitational force on the drop increases with the drop mass and is proportional to the cube of the diameter. Hence, u_t increases with drop diameter approximately linearly for small d, where the drag coefficient is proportional to the inverse of the drop Reynolds number. However, for large d, the drag coefficient changes with Reynolds number in a more complicated fashion, and the relationship between the fall speed and d becomes nonlinear. The functional relationship between u_t and drop diameter has been a subject of research for some time, recently motivated by the necessity of knowing this function when converting the DSD obtained from radar scatter data into rain rates (see equation (6)). A variety of relationships giving u_t as a function of raindrop diameter d have been formulated. A selection of these are plotted in Figure 11 and listed in Appendix A. Velocities range up to 9 m s^{-1} for the largest raindrop sizes.

The terminal velocity is affected by several aspects of drop morphology, including drop shape, characteristics of the wake, and drop oscillation dynamics. Because of this dependence, a review of the literature on this subtopic is presented here.

Experimental studies of u_t for water drops began in the early twentieth century, with perhaps the earliest work being that due to *Lenard* [1904]. Other investigators of this period were *Schmidt* [1909], *Liznar* [1914], *Flower* [1928], and *Laws* [1941]. In 1949, *Gunn and Kinzer* [1949] conducted a careful investigation of raindrop u_t, taking great care to accurately measure the mass and speed of the drop. As noted by these authors, the earlier literature used relatively coarse methods for mass measurement, for example, relying on the size of the spot created by a drop after it impacted a specially treated piece of paper [*Schmidt*, 1909; *Lenard*, 1904] or by allowing drops to fall into fine flour which was subsequently measured [*Laws*, 1941]. *Gunn and Kinzer* [1949], on the other hand, measured drop masses in two ways. For large diameters, drops

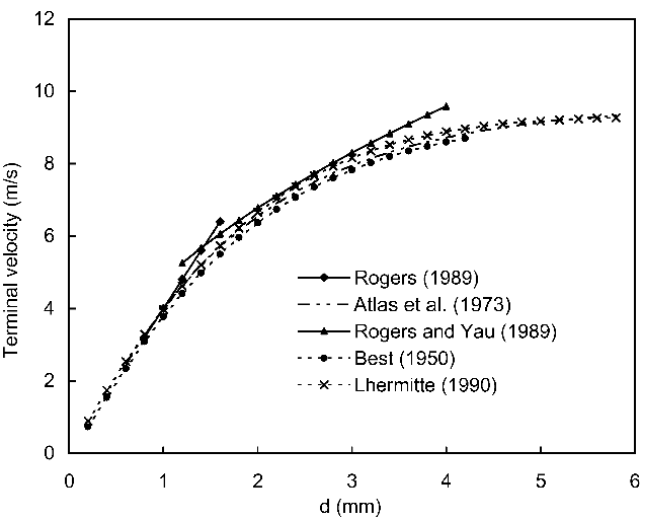

Figure 11. Terminal fall velocity u_t in m s^{-1} as a function of drop diameter d (mm) given by various authors (see Appendix A).

were carefully collected and their mass measured using a precise chemical balance. For small diameters, the drops were captured in a dish containing high quality vacuum-pump oil and the diameter then measured using a microscope. This latter method had the advantage of preventing any evaporation of the drop, since it was encased in an oil medium (an important advantage for small drops, where a small amount of evaporation could result in large errors). Although the data acquired by Gunn and Kinzer suffered from other problems (e.g., evaporation while falling through a 50% relative humidity environment), it is still of high quality, even by today's standards, and is frequently cited.

In the late 1960s, Beard and coworkers published several works pertaining to u_t. *Beard and Pruppacher* [1969] studied u_t for water drops in a special wind tunnel designed to levitate drops in an airflow of known speed, at a controlled temperature and relative humidity. These authors point out that the data of Gunn and Kinzer were obtained at a relative humidity of 50%. *Beard and Pruppacher* [1969] measured u_t for drop diameters ranging from 10 to 475 μm at a relative humidity of 100%, but found no significant deviation from Gunn and Kinzer's data (although they did observe very slight deviations, which they attributed to evaporation in Gunn and Kinzer's experiments). These authors also computed drag coefficients and showed that for a drop Reynolds number Re less than 200, the drag coefficient for drops deviated insignificantly from those for solid spheres. They concluded that for this range of Re, drops are essentially round, although a subsequent photographic study due to *Pruppacher and Beard* [1970] showed this conclusion to be strictly true only for $Re < 20$. *Pruppacher and Beard* [1970] also showed the velocity at the drop surface to be only about 1% of the terminal velocity. Hence, it is unlikely that the internal flow significantly affects the value u_t.

An interesting aspect of the variation of u_t with drop diameter concerns the behavior of drops in vertical updrafts during convective precipitation. A vertical updraft with velocity u_u will allow drops having a terminal velocity $u_t > u_u$ to fall, while those having smaller terminal velocities ($u_t < u_u$) will remain suspended, unable to fall. A model developed by *Srivastava and Atlas* [1969] shows that a convective cloud having an assumed linearly increasing updraft, capped by a linearly decreasing updraft, will cause a horizontal and vertical size-sorting of drops. Data obtained from aircraft support the results of this model [*Carbone and Nelson*, 1978; *Rauber et al.*, 1991; *Szumowski et al.*, 1998; *Atlas and Ulbrich*, 2000]. Measurements obtained from a Doppler radar further develops these ideas, showing how the relationship between the updraft and the variation in u_t with drop diameter results in a sorting of drop sizes in both the vertical and horizontal direction of the cloud structure [*Kollias et al.*, 2001].

Another interesting aspect of the literature on terminal velocity concerns the acceleration of drops to u_t. This acceleration can be characterized by the time and/or distance required for a drop to reach some fraction of u_t. This is an important topic, since raindrops are frequently perturbed from a stable fall velocity by a change in local air velocity as they fall and/or by collision with other drops. Knowing the time/distance needed to achieve u_t is also important in the design of drop towers.

Laws [1941] observed, in artificially generated drops, that the distance required for a drop to achieve 95% of its terminal fall velocity z_{95} did not increase monotonically with drop diameter, but rather achieved a maximum at a diameter of 4 mm (Laws presents z_{95} data for drop diameters d = 1, 2, 3, 4, 5, 6 mm, which have values of z_{95} = 2.2, 5.0, 7.2, 7.8, 7.6, 7.2 m). Laws explains this result using plots of drop velocity versus fall distance showing that for large drops (specifically d = 6.1 mm), the plot has a maximum, rather than asymptotically approaching u_t. That is, the drop exceeds u_t and then decelerates to u_t. This, in turn, he postulates, is due to a delay in the time required for the drop shape to attain an equilibrium (flattened) shape at a given instantaneous velocity. That is, near terminal velocity, the drop is closer to spherical than it should be for that given velocity, and hence accelerates further, achieving a velocity greater than terminal. The drop shape then becomes flatter, causing the drop to slow down and relax to its true terminal velocity. This phenomenon occurs only for large drops, since these exhibit significant deviations from spherical. Laws supports his argument with one presented by *Lenard* [1904], who similarly postulated that a time lag in achieving drop shape allowed drops to remain more spherical at a given instantaneous velocity than they would be at steady state, allowing them to accelerate to a velocity larger than u_t. Lenard furthermore argued that this phenomenon would be best explained if the drop shape was significantly affected by internal circulation within the drop, since the acceleration of the internal drop fluid would take a significant amount of time due to its mass. While a delay in attaining a steady state drop shape for a given velocity is certainly a factor in how a drop accelerates to its steady state velocity, Lenard's argument seems problematic to the present authors, since internal circulation in the drop results in a drop surface velocity, which reduces the net drop-to-air velocity, which would contribute to a continually decreasing drag force as the internal circulation flow ramps up, which one would expect to contribute to a monotonic approach to terminal velocity. *Beard* [1977a] also notes that the work of *Foote* [1969] shows that internal circulation results in less distortion, not more, further ruling out internal circulation as the result of Laws' and Lenard's observations. The work

of *LeClair et al.* [1972] shows little effect of internal circulation on the drag on a drop for cases where the drop is nominally spherical.

Wang and Pruppacher [1977] revisit the problem of acceleration to terminal velocity through experiments in a drop tower and via the development of a theoretical method to compute the acceleration to terminal velocity. The theoretical and experimental results of *Wang and Pruppacher* [1977] do not reveal a maximum in their plots of instantaneous velocity versus fall distance. However, they do show a maximum in their plots of t_{99} (as well as z_{99}) versus drop size at a diameter of 3.2 mm, a pressure of 1000 mb, and a temperature of 20°C. This is similar to Laws' peak in t_{95} at a diameter of 4 mm. Considering the sparsity of Laws' data and the relatively crude methods by which it was attained, one should probably conclude agreement between his study and that of Wang and Pruppacher. However, the lack of a peak in the instantaneous velocity versus fall distance of *Wang and Pruppacher* [1977] requires a different explanation for the peak in t_{99} that they observe. Such an explanation of Wang and Pruppacher's results is probably best given by *Beard* [1977a] who notes that above a diameter of about 1 mm, drops begin to deviate significantly from sphericity, and as the diameter increases beyond 1 mm, this occurs earlier during the drop fall, thereby reducing t_{99} and z_{99} for $d > 1$ mm drops.

The studies described above focus almost exclusively on the terminal velocity of a single drop. In most analytical investigations and in most laboratory studies, the goal is to observe drops in the absence of air velocity fluctuations (turbulent or otherwise), collisions with other drops, and in the absence of evaporation or condensation. Of course, during actual rain, all of these effects are in play and can result in a drop velocity that differs from the terminal velocity predicted via analysis or from laboratory experiments. These factors will all affect drop velocity in that they perturb the drop from a nominally steady state condition into a transient one. It should be made clear that these effects do not "change" the value of terminal velocity. Rather, these effects simply cause a drop to undergo a transient and reapproach terminal velocity. This terminal velocity may be "new" only if the drop has changed somehow, e.g., it has increased in size due to collision with a smaller drop. There is some evidence to suggest that during heavy rain fall, many or perhaps even most drops do not achieve terminal velocity for any significant period of time. In other words, the number of drop collisions and the constantly changing velocity field of the air cause such a changing environment that drops are continually accelerating or decelerating to a new speed. This is suggested, for example in the work of *Montero-Martínez et al.* [2009] who show that for high rain rates ($R > 84$ mm h^{-1}), up to 50% of 0.44 mm diameter drops traveled at speeds greater than the predicted terminal velocity and that for a drop having a diameter of 0.24 mm, up to 80% of these drops are superterminal.

For very small drop diameters, mild deviations from the continuum flow assumption can result in errors in terminal velocity relations obtained for larger drops. As pointed out by *Beard* [1976], even though the terminal velocities of drops on the order of a micron are extremely small, they are needed to compute collision efficiencies, and this author computed a revised terminal velocity equation for these very small drops. Similar work was done by *Beard* [1977b] who accounted for noncontinuum effects and also presented an adjustment for sea-level terminal velocity equations that accounted for changes in terminal velocity due to temperature and pressure, permitting simple corrections to terminal velocity for drops over a range of altitude.

Ryan [1976] studied the effect of surfactants on the terminal velocity of drops using a drop levitation tunnel. Reduction in the drop surface tension by surfactants caused drops to deform (at equivalent drop volume) and flatten, reducing the terminal velocity. For example, using surfactants to reduce the surface tension to 17 dynes cm^{-1}, Ryan found that u_t for a drop having an equivalent spherical diameter of 3 mm dropped by more than 20%.

Due to the changes in air properties with altitude, the terminal velocity of a drop is a function of height above sea level. Several researchers have quantified this and developed equations for u_t in terms of air properties. These equations are sometimes reformatted to provided u_t in terms of altitude or barometric pressure. Examples of such studies include *Battan* [1964], *Cornford* [1965], *Foote and DuToit* [1969], *Berry and Pranger* [1974], *Beard* [1976], *Wang and Pruppacher* [1977], and *Beard* [1977b].

Note that the effect of freezing on u_t and velocities of partially or fully frozen drops is not considered here, and the effect of electrostatic forces on u_t is briefly discussed in the next section.

6. ELECTROSTATIC EFFECTS

Drops in many clouds are electrically charged at an early stage of the cloud life cycle when exposed to the external electric fields present in electrically charged clouds [*Rasmussen et al.*, 1985; *Despiau and Houngninou*, 1996]. Consequently, these drops are subject to electrostatic forces. The primary effects of electrostatic forces on the raindrop morphodynamics are threefold: (1) distortion, (2) fall speed alteration, and (3) disruption of raindrop stability. Due to scarce data on the behavior of charged drops falling steadily in an ambient field, our understanding of the effects of electrostatic forces on raindrop morphodynamics is limited mainly to simplified theoretical and numerical models

[*Coquillat and Chauzy*, 1993; *Beard et al.*, 1989a; *Chuang and Beard*, 1990; *Zrnić et al.*, 1984].

For an electrically distorted raindrop, the dependence of the drop shape on the electric field is highly nonlinear due to the coupling between the surface electrostatic stress and the aerodynamic distortion [*Chuang and Beard*, 1990]. The surface electrostatic stress caused by the electrical charge will tend to oppose surface tension, with the charge concentrated in regions of highest curvature. When the water drop is small and maintains its spherical shape, the electrical charge uniformly distributes over its surface [*Kamra et al.*, 1991]. However, since the maximum curvature of large, distorted drops is located just below the waist, these drops will be extended horizontally under the influence of electric charge. Thus, the effect of large surface charge is increased oblateness [*Chuang and Beard*, 1990]. On the other hand, an uncharged drop situated in an electric field will become elongated along the direction of the field [*Bhalwankar and Kamra*, 2007; *Coquillat et al.*, 2003]. Therefore, oblateness of a drop increases (decreases) in the presence of a horizontal (vertical) electric field compared to the equilibrium shape of the same-size drop in the absence of an electric field. Numerical simulations of *Coquillat et al.* [2003], later confirmed by experimental observations of *Bhalwankar and Kamra* [2007], showed that horizontal electric fields are more efficient than vertical ones in deforming the drop. This is because in a horizontal electric field, aerodynamic and electrostatic forces act together to distort the drop, whereas in a vertical field these forces counteract to suppress distortion effects.

In a recent vertical wind-tunnel study, *Bhalwankar and Kamra* [2009] investigated the effect of contaminants on the shapes of uncharged raindrops in a horizontal electric field, a simulation of contaminated raindrops in thunderstorms over large, polluted cities. *Bhalwankar and Kamra* [2009] observed that contaminated raindrops were more distorted (i.e., their oblateness increased) with respect to distilled water drops, and the observed difference in distortion increased with increasing electric field. They explained this observation as a consequence of the increased electrical forces acting on the drop due to the increase in the electrical conductivity of water when it is polluted. Based on their experimental results, *Bhalwankar and Kamra* [2009] provided brief qualitative discussions on the modification of raindrop size distribution and lightning activity in clouds formed over large cities. Further research is needed on electrostatic effects on contaminated raindrops, especially in vertical electric fields that are considered to be representative of thundercloud conditions, for quantitative conclusions.

When the drop is in motion, the combined effect of aerodynamic and electrostatic forces determines the raindrop shape. For example, *Chuang and Beard* [1990] reported that uncharged drops falling in strong vertical electric fields, representative of thundercloud conditions [*Rasmussen et al.*, 1985], show a pronounced extension of the upper pole and an enhanced flattening of the lower pole (i.e., triangular-like drop profiles) due to increased fall speed of electrostatically stretched drops. A summary of the calculations performed by *Chuang and Beard* [1990] are provided in Figure 12.

Electrostatic forces experienced by charged raindrops in a thundercloud may alter the force balance between the gravitational and aerodynamic forces acting on the raindrop. As a result, the terminal velocity of a raindrop under electrostatic effects may significantly deviate from the terminal velocity of a raindrop with the same diameter but isolated from electrostatic effects [*Coquillat and Chauzy*, 1993]. The raindrop terminal velocity is affected by the combined effects of the charge that the raindrop carries and

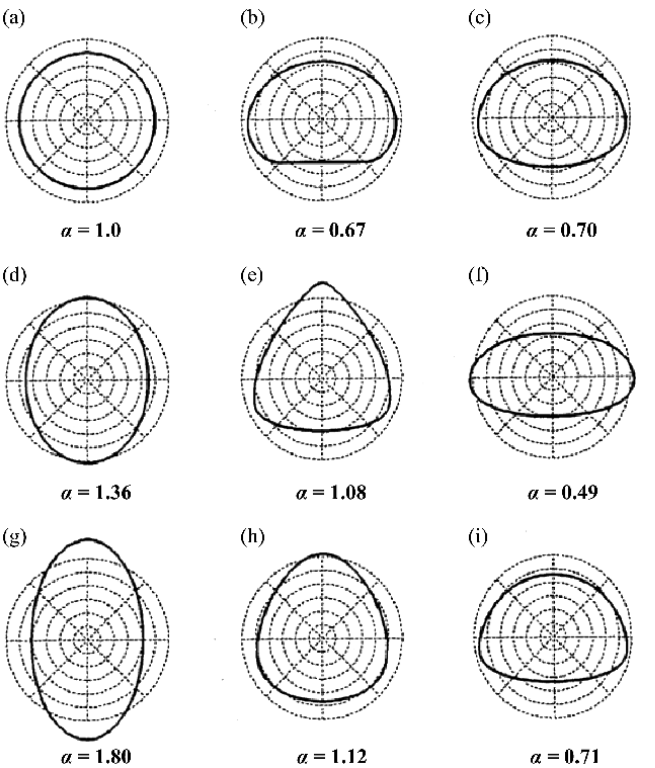

Figure 12. Shapes and axis ratios for a 5-mm drop with various distortion effects: (a) stationary drop (surface tension only); (b) sessile drop (surface tension and hydrostatic stress); (c) raindrop (surface tension, hydrostatic, and aerodynamic stresses); (d) stationary drop in vertical electric field; (e) uncharged raindrop in vertical electric field; (f) charged raindrop; (g) stationary drop in vertical electric field with largest possible distortion; (h) raindrop with maximum field charge combination with upward electric force; (i) same as Figure 12h with downward electric force. From *Chuang and Beard* [1990]. Copyright 1990 American Meteorological Society.

the electric field in which it moves. The effect of electrostatic forces may be to increase (e.g., positively charged raindrops in a negative vertical electric field) or to decrease (e.g., negatively charged raindrops in a negative vertical electric field) the raindrop terminal velocity depending upon the polarity of charge on the raindrop and the direction of the electric field [*Kamra*, 1975]. An important consequence of raindrop terminal velocity variations due to electrostatic effects is on the charge separation mechanism, which is assumed to be responsible for the negative electric fields that may cause lightning flashes in thunderclouds. The charge separation mechanism and the role of terminal velocity deviations of charged raindrops in this mechanism is out of the scope of this chapter, and the interested reader is kindly referred to *Kamra* [1970] and/or *Kamra* [1975]. It should be noted that induced velocity perturbations result in a change in the aerodynamic pressure around the raindrop, one of the primary factors governing the drop shape as discussed earlier. As a result, the simultaneous and accurate determination of the shape and the terminal velocity of a charged raindrop in an electric field are difficult because of the high interdependence of both parameters [*Coquillat and Chauzy*, 1993]. This aspect of raindrop dynamics is an open area of research.

Zrnić et al. [1984], extending the model of *Green* [1975] for describing the drop shape by including electrostatic effects, reported that commonly observed electric fields in clouds have only a modest effect on drop shape. *Rasmussen et al.* [1985] argued against this finding because of the discrepancy between Zrnić's predictions and wind-tunnel observations for the shape and disruption values of raindrops by *Dawson and Richards* [1970] and *Richards and Dawson* [1971]. Later, Zrnić's prediction was supported by model predictions of *Beard et al.* [1989a] and *Chuang and Beard* [1990], who added that somewhat stronger fields for highly charged raindrops can lead to instability/disruption. *Coquillat and Chauzy* [1993] predicted quite high field intensities for the disruption of uncharged raindrops, but they noted that the combination of field and net charge may lead to probable disruptions of charged raindrops in ambient fields of the order of those commonly measured in nature.

Accurate quantitative information on the electric field amplitude required for drop disruption remains incomplete. Moreover, the question of whether typical electrical fields in thunderclouds are sufficient to cause disruptions of drop stability is still a subject of debate. A classical reference for instability (i.e., disruption) of a drop acted upon by electrical forces is the work of *Taylor and Acrivos* [1964], which provided the following theoretical criterion for the onset of drop instability,

$$F\left(\frac{r_0}{\sigma}\right)^{1/2} = 1.63. \tag{24}$$

Here F is the value of critical electric field in esu, r_0 is the undistorted drop radius in cm, and σ is the surface tension in dynes cm^{-1}. Although Taylor's criterion agrees well with experimental observations reported by different authors, *Kamra et al.* [1993] reported a significantly lower critical electric field value for the onset of drop instability. Kamra et al. argued that the difference between their observations and those reported by others is because of long exposure of the freely suspended drops to the electric fields in their vertical wind-tunnel setup. This discrepancy between the observations of Kamra et al. and Taylor's criterion is later followed up by *Georgis et al.* [1997], who studied the onset of drop instability for free-falling drops at terminal velocity in a horizontal electric field. Georgis et al. reported a large discrepancy between their observations and those of Kamra et al., claiming they were possibly due to the experimental conditions of Kamra et al., specifically the high turbulence levels inherent to vertical wind tunnels. *Coquillat et al.* [2003] numerically studied the critical electric field for the onset of drop instability. Their simulation results showed good agreement with the experimental observations of *Georgis et al.* [1997]. However, the numerical simulations of Coquillat et al. did not take into account the effect of ambient turbulence and drop oscillations. As turbulence and drop oscillations are keys to the drop instability, Coquillat et al. noted that actual instability onset values in thundercloud conditions may be closer to the results by *Kamra et al.* [1993].

Bhalwankar and Kamra [2007] considered the stabilizing and destabilizing effects of ambient electric fields on uncharged raindrops. They suggested that vertical electric fields stabilize distorted drops by stretching along the drop vertical axis (reducing oblateness), whereas horizontal electric fields destabilize drops by stretching the drop along its horizontal axis, increasing oblateness. Based on this argument, Bhalwankar and Kamra discussed effects of electric field direction, which may differ between clouds and in different regions of the same cloud, on raindrop size distributions and raindrop growth rates.

Kamra et al. [1991] discussed the role of oscillations in the disruption of charged drops and postulated a destabilizing effect due to coupling between a surface charge density shift and drop shape distortion associated with oscillations. In the case of contaminated drops, such as those existing in rain over large cities, dissolved pollutants in the drop tend to reduce the amplitude of drop oscillations through an increase in surface tension. This effect of pollutants enhances drop stability against electric forces, which tend to break up the drops [*Bhalwankar and Kamra*, 2009]. Hence, a possible consequence of pollutant presence is to broaden the raindrop size distribution.

7. EXPERIMENTAL TECHNIQUES

Given the complex nature of the governing equations (see discussion in section 2), numerical and analytical studies on raindrop morphodynamics are challenging, thus experimental observations have played a critical role in studying raindrop morphodynamics. Experimental work on the shape, terminal velocity, and stability of raindrops began with *Lenard* [1887, 1904], who made nighttime flash photography observations and investigated the role of surface tension and internal circulation on drop shape using a wind tunnel. Prior work focused on pendant and sessile drops, likely owing to the experimental challenges of obtaining accurate measurements of unsupported, floating or falling drops. Later, *Flower* [1928] and *Laws* [1941] reported terminal velocity calculations, while the high-speed photographs of *Edgerton and Killian* [1939] and *Blanchard* [1950] further explored drop behavior. *McDonald* [1954b] outlined the available literature and also examined the photographs of *Magono* [1954] to deduce the distribution of aerodynamic pressure around the drop surface and show the distorting effects of flow separation. Figure 9 presents a representative selection of experimental data from the works outlined here, all of which depict the wide scatter indicative of oscillations, discussed in section 4.

Some aspects of raindrop morphodynamical behavior can be simulated in the laboratory, either using levitated or free-falling drops. Levitated drop studies are conducted using specially constructed vertical wind tunnels whereby drops are observed as they float in upward-oriented flow. Most wind tunnel designs condition the airflow using baffles or screens to reduce turbulence; however, more sophisticated tunnels may incorporate temperature and humidity controls [*Pruppacher and Beard*, 1970; *Mitra et al.*, 1992], electrical fields [*Kamra et al.*, 1986], or flow-visualization techniques [*Saylor and Jones*, 2005] in addition to the primary shape or frequency sensing method.

Data from the wind tunnel work of *Pruppacher and Beard* [1970] contributed to the important semiempirical drop shape model of *Pruppacher and Pitter* [1971], as well as an axis ratio relationship that was recently validated by *Thurai and Bringi* [2005]. *Beard and Pruppacher* [1969] also used wind tunnel measurements to develop a more sophisticated terminal velocity formula based on drag coefficients that improved upon the available literature, citing errors in the works of *Gunn and Kinzer* [1949], *Laws* [1941], and *Imai* [1950]. More recently, *Szakall et al.* [2009], using shape and axis ratio measurements of 2.5 mm $\leq d \leq$ 7.5 mm drops, found drop shapes to match the equilibrium model of *Beard and Chuang* [1987] in addition to oscillation behavior further outlined in section 4. *Jones and Saylor* [2009] also reported mean axis ratio measurements matching the *Beard and Chuang* [1987] equilibrium model, a curious result considering the shift in mean axis ratio usually reported from drop measurements [*Andsager et al.*, 1999]. *Bhalwankar and Kamra* [2009] and *Rasmussen et al.* [1985] have also utilized wind tunnels to study the effects of electrical fields and charging on drop shape and breakup behavior. Wind tunnels have also been utilized by *Blanchard* [1948], *Brook and Latham* [1968], *Nelson and Gokhale* [1972], *Musgrove and Brook* [1975], and *Goodall* [1976] to obtain quantitative observations of drop oscillation frequency from image measurements or microwave backscatter; some of these data are shown in Figure 8.

Free-falling drop studies are conducted using towers whereby drops fall from a height sufficient to approach terminal velocity. Drop towers consist of a drop production apparatus situated above cameras or sensors designed to measure shape or oscillation behavior. To accurately simulate real raindrop behavior, consideration should also be given to the fall height required to dampen anomalous surface dynamics resulting from drop generation [*Beard and Kubesh*, 1991] and for an oscillation steady state to fully develop [*Andsager et al.*, 1999]. Though outdoor experiments may provide additional height over enclosed arrangements, ambient winds must be monitored so that fall trajectories remain aligned with the instrument measurement volume or camera field of view.

Experimentation with falling drops has been an elemental technique in raindrop microphysics research, from the early studies mentioned above to the more recent work described here. For example, *Beard et al.* [1991] in their 4-m fall tower study of 0.70 mm $\leq d \leq$ 1.54 mm drops, largely determined what is known about drop oscillations, wakes, and fall behavior. The mean and scatter in their axis ratio measurements indicated distinct oscillation behavior at specific sizes, suggestive of the long-postulated causality between asymmetric oscillations and drop wake vortex shedding. *Andsager et al.* [1999] used a similar but taller 25-m arrangement to measure axis ratios of 2.5 mm $\leq d \leq$ 4 mm drops at discrete fall distances, reporting time development of oscillations even after drops had reached terminal velocity. *Thurai and Bringi* [2005] also obtained measurements of drop shape from an 80-m tower, finding good agreement with the equilibrium shapes due to *Beard and Chuang* [1987], implying an absence of the transverse oscillations evidenced in other data.

Measurements of oscillation frequency have been obtained from falling drop arrangements, wind tunnel experiments, and observations of real rain. *Brook and Latham* [1968] and *Goodall* [1976], for example, utilized microwave scattering to measure oscillation frequencies of drops floating in a wind tunnel. In a falling drop study, *Beard and Kubesh* [1991]